Geophys. J. Int. () ,

A Rayleigh-Ritz method based approach to computing seismic normal modes in the presence of an essential spectrum

Jia Shi[1], Ruipeng Li[2], Yuanzhe Xi[3], Yousef Saad[4] and Maarten V. de Hoop[5]

[1] *Department of Earth, Environmental and Planetary Sciences, Rice University, USA. Email: jia.shi@rice.edu*

[2] *Center for Applied Scientific Computing, Lawrence Livermore National Laboratory, Livermore, CA, USA*

[3] *Department of Mathematics, Emory University, Atlanta, GA, USA*

[4] *Department of Computer Science and Engineering, University of Minnesota, MN, USA*

[5] *Simons Chair in Computational and Applied Mathematics and Earth Science, Rice University, Houston, TX, USA*

SUMMARY

A Rayleigh-Ritz with Continuous Galerkin method based approach is presented to compute the normal modes of a planet in the presence of an essential spectrum. The essential spectrum is associated with a liquid outer core. The presence of a liquid outer core requires the introduction of a mixed Continuous Galerkin finite-element approach. Our discretization utilizes fully unstructured tetrahedral meshes for both solid and fluid domains. The relevant generalized eigenvalue problem is solved by a combination of several highly parallel, computationally efficient methods. Self-gravitation is treated as an N-body problem and the relevant gravitational potential is evaluated directly and efficiently utilizing the fast multipole method. The computational experiments are performed on constant elastic balls and the isotropic version of the preliminary reference earth model (PREM) for validation. Our proposed algorithm is illustrated in fully heterogeneous models including one combined with crust 1.0.

1 INTRODUCTION

Planetary normal modes are important for studying the dynamic response to sources including earthquakes along faults, meteorite impacts, postseismic relaxation, as well as for analyzing and computing surface and body waves (Dahlen & Tromp 1998; Lognonné 2005). The relatively low-lying, but many eigenfrequencies in the spectrum of a planet contain critical information about its large-scale structure and provide constraints on heterogeneity in composition, temperature, and anisotropy.

For a review of Earth's free oscillations, we refer to Woodhouse & Deuss (2007). Current standard approaches to computing the point spectrum and associated normal modes have several limitations. Assuming spherical symmetry, the problem becomes one-dimensional and the computations in such models using `MINEOS` (Woodhouse 1988; Masters et al. 2011) are still common practice; these are then typically used in a perturbation theory to include angular heterogeneities. Utilizing the normal modes in a spherically symmet-

ric model as a basis leads to a full-mode coupling approach (Deuss & Woodhouse 2001, 2004; Al-Attar et al. 2012). Such a Rayleigh-Ritz type approach works well under the assumption of weak angular heterogeneity, in particular, assuming that the fluid-solid boundaries are exact spheres. Indeed, this basis does not fit any non-spherically symmetric discontinuities. A separation of the essential spectrum needs to be carried out carefully. We discuss this approach in Appendix A.

In this paper, we revisit the work of Buland & Gilbert (1984). They encountered several complications that we overcome by characterizing and separating the essential spectrum and introducing the mixed finite-element method (FEM) for fully heterogeneous terrestrial planets. In a separate paper (Shi et al. 2018), we introduce a highly parallel algorithm for solving the generalized eigenvalue problem resulting from our analysis.

Self-gravitation manifests itself in the incremental gravitational potential because the density change with displacement needs to be included for computing long-period modes. We utilize the fundamental solution and treat the self-gravitation as an N-body problem. We then apply the fast multipole method (FMM) (Greengard & Rokhlin 1997; Gimbutas & Greengard 2011; Yokota 2013), which reduces the algorithm complexity significantly, to compute both the reference gravitational and the incremental gravitational potentials. Alternatively, one can apply a finite-infinite element method (Zienkiewicz et al. 1983; Burnett 1994) for modeling unbounded domain problems to approximate the far-field of Poisson's equation. More recently, the spectral-infinite-element method (Gharti et al. 2018) has been developed for incorporating gravity. While our eigensolver (Shi et al. 2018) only takes matrix-by-vector products, any suitable schemes, such as FMM or infinite-element methods, can be used in our computational framework.

The outline of this paper is as follows. In Section 2, we revisit the physics of normal mode seismology and design the proper weak formulation of the elastic-gravitational system and the separation of the essential spectrum. In Section 3, we introduce the Continuous Galerkin mixed FEM and obtain the corresponding matrix equations. In Section 4, we study the computation of the reference gravitational field and self-gravitation using the FMM. In Section 5, we discuss the resulting generalized eigenvalue problem and eigensolvers. In Section 6, we present and validate our 3D computations using constant elastic balls and an isotropic PREM with and without self-gravitation. We calculate normal modes of two fully 3D Earth models including one with a complex 3D crust. The visualization of various modes of PREM can be found in Appendix B. In Section 7, we summarize our current work and discuss future directions of research.

2 WEAK FORMULATION: THE ELASTIC-GRAVITATIONAL SYSTEM

In this section, we present the elastic-gravitational system of equations of a non-rotating planet in the weak form; see Dahlen & Tromp (1998); de Hoop et al. (2015) for the strong formulation. Since Earth contains both solid and fluid regions, we use it as one of our examples and then generalize our approach to study other planets.

2.1 Natural subdomains and computational meshes

Following the notation in de Hoop et al. (2015), a bounded set $\tilde{X} \subset \mathbb{R}^3$ is used to represent the interior of the Earth, with Lipschitz continuous exterior boundary $\partial\tilde{X}$. The exterior boundary $\partial\tilde{X}$ contains fluid (ocean) surfaces $\partial\tilde{X}^{\mathrm{F}}$ and solid surfaces $\partial\tilde{X}^{\mathrm{S}}$. We subdivide the set $\tilde{X}$ into solid regions Ω^{S} and fluid regions Ω^{F}. The fluid regions contain the liquid outer core Ω^{OC} and the oceans Ω^{O}. The solid regions can be further subdivided into the crust and mantle Ω^{CM} and the inner core Ω^{IC}. We use Σ to represent the interfaces between these subregions. In summary,

$$\tilde{X} = \Omega^{\mathrm{S}} \cup \Omega^{\mathrm{F}} \cup \Sigma \cup \partial\tilde{X},\ \partial\tilde{X} = \partial\tilde{X}^{\mathrm{S}} \cup \partial\tilde{X}^{\mathrm{F}},\ \Omega^{\mathrm{S}} = \Omega^{\mathrm{CM}} \cup \Omega^{\mathrm{IC}},\ \ \Omega^{\mathrm{F}} = \Omega^{\mathrm{OC}} \cup \Omega^{\mathrm{O}}.$$

The interior interfaces can further be subdivided into three categories: interfaces between two fluid regions Σ^{FF}, interfaces between two solid regions Σ^{SS}, and interfaces between fluid and solid regions Σ^{FS}. We can subdivide Σ^{FS} into two major interfaces: internal interfaces $\Sigma^{\mathrm{FS}}_{\mathrm{int}}$ and the bottom interface $\Sigma^{\mathrm{FS}}_{\mathrm{O}}$ of the oceans. The internal interfaces include interfaces between the lower mantle and the outer core Σ^{CMB}, which is known

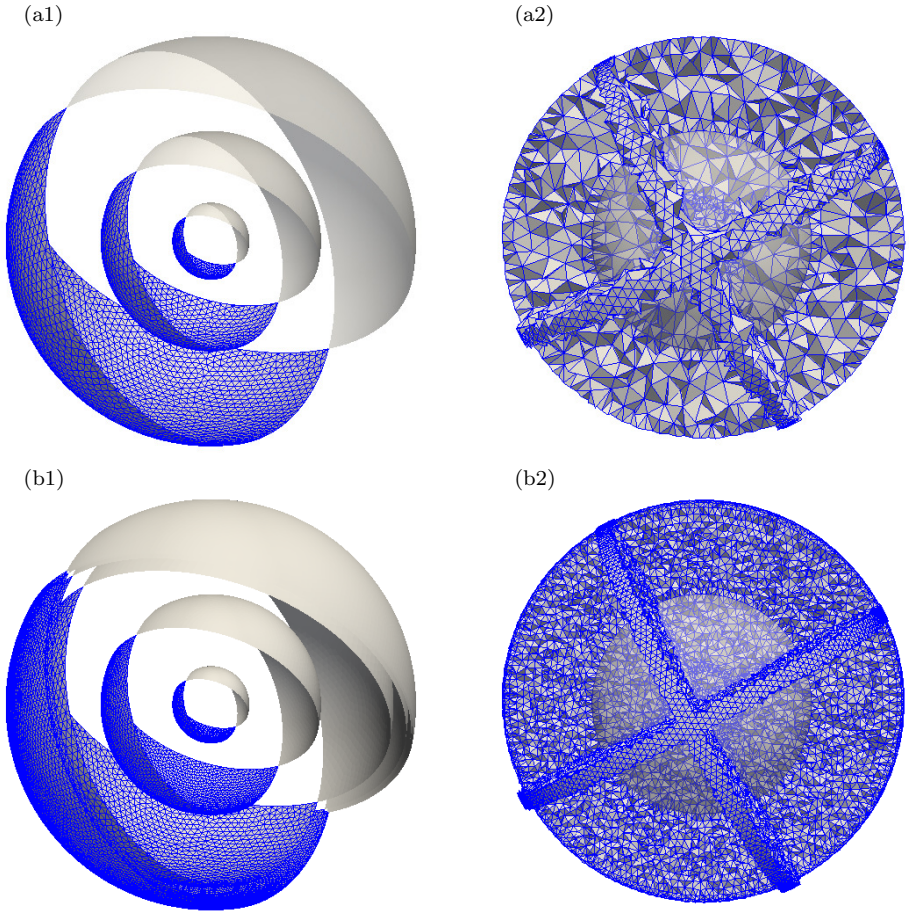

Figure 1. Illustration of different meshes. (a1) Three triangularized surface meshes; (a2) A tetrahedral mesh with 100k elements that is generated from (a1); (b1) Seven triangularized surface meshes; (b2) A tetrahedral mesh with 1 million elements that is generated from (b1). The light surfaces in (b1) and (b2) denote the CMB.

as the Core Mantle Boundary (CMB); the interface between the outer core and the inner core is denoted as Σ^{ICB}, which is known as the Inner Core Boundary (ICB). Thus,

$$\Sigma = \Sigma^{\mathrm{SS}} \cup \Sigma^{\mathrm{FF}} \cup \Sigma^{\mathrm{FS}},\ \Sigma^{\mathrm{FS}} = \Sigma^{\mathrm{FS}}_{\mathrm{int}} \cup \Sigma^{\mathrm{FS}}_{\mathrm{O}},\ \Sigma^{\mathrm{FS}}_{\mathrm{int}} = \Sigma^{\mathrm{CMB}} \cup \Sigma^{\mathrm{ICB}}.$$

Since a general terrestrial planet may contain multiple complex discontinuities associated with different geological and geodynamical features, utilization of a flexible, fully unstructured tetrahedral mesh will be natural. We discretize the major discontinuities using triangulated surfaces that are generated via `distmesh` (Persson & Strang 2004) and then build up the Earth model using an unstructured tetrahedral mesh via `TetGen` (Si 2015). In Fig. 1 we illustrate the interfaces and meshes with one hundred thousand and one million elements. The techniques show great flexibility and can provide models with multiple resolutions. In Figs. 2, we illustrate a 3D Earth model built on a tetrahedral mesh. In Fig. 2(a), we show the Moho interface that is constructed using an unstructured triangular mesh. The color shows the depth and the black lines are the edges of triangles. In Fig. 2(b), we illustrate the 3D V_P model based on MIT's mantle tomographic results (Burdick et al. 2017) and crust 1.0 (Laske et al. 2013). The core model is based on PREM.

2.2 The basic equations

Here, we revisit seismology of the non-rotating Earth and set up the strong form of the elastic-gravitational equations with all the necessary boundary conditions.

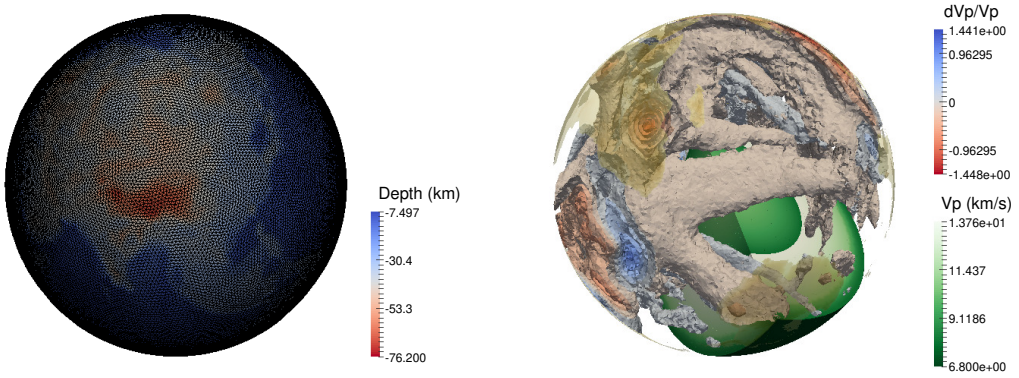

(a) Moho (b) MIT V_P model

Figure 2. A 3D Earth model built using MIT tomographic results (Burdick et al. 2017) and crust 1.0 (Laske et al. 2013). (a) A triangle mesh built for Moho. The color indicates the depth below the reference surface of the Earth. The bottom of the Tibet Plateau is shown. (b) MIT mantle V_P model built on a tetrahedral mesh. The V_P model and the contours of $\mathrm{d}V_P/V_P$ (%) are shown.

Given the reference density ρ^0 and the gravitational constant G, we let Φ^0 denote the gravitational potential, satisfying

$$\Delta\Phi^0 = 4\pi G\rho^0, \tag{1}$$

and $S(u)$ denote the Eulerian perturbation of the Newtonian potential associated with the displacement, u, satisfying

$$\Delta S(u) = -4\pi G\nabla\cdot(\rho^0 u). \tag{2}$$

The elastic-gravitational system of the non-rotating Earth has the form

$$-\rho^0\omega^2 u = \nabla\cdot T^{\mathrm{PK1}} - \rho^0 u\cdot\nabla\nabla\Phi^0 - \rho^0\nabla S(u), \tag{3}$$

where $T^{\mathrm{PK1}} = \Lambda^{T^0}:\nabla u$ denotes the first Piola-Kirchhoff stress tensor with the elasticity tensor Λ^{T^0}. Here, Λ^{T^0} is defined as

$$\Lambda^{T^0}_{ijkl} = c_{ijkl} + \frac{1}{2}\left(T^0_{ij}\delta_{kl} + T^0_{kl}\delta_{ij} + T^0_{ik}\delta_{jl} - T^0_{jl}\delta_{ik} - T^0_{jk}\delta_{il} - T^0_{il}\delta_{jk}\right),$$

where c is the elastic stiffness tensor and T^0 satisfies the mechanical equilibrium given by the static momentum equation,

$$\nabla\cdot T^0 = \rho^0\nabla\Phi^0. \tag{4}$$

In Table 1, we show all the boundary conditions for the elastic-gravitational system (3) as in de Hoop et al. (2015), where ν denotes the normal vector; $\nabla^\Sigma\cdot$ is the surface divergence and W is the Weingarten operator.

We transform (3) to

$$-\rho^0\omega^2 u = \nabla\cdot T^{\mathrm{L1}} - \nabla\cdot(u\cdot\nabla T^0) - \rho^{\mathrm{E1}}\nabla\Phi^0 - \rho^0\nabla S(u), \tag{5}$$

where $\rho^{\mathrm{E1}} = -\nabla\cdot(\rho^0 u)$ denotes the first-order Eulerian density perturbation and $T^{\mathrm{L1}} = \Upsilon^{T^0}:\nabla u$ denotes

boundary types	linearized boundary conditions
Earth's free surface, $\partial\tilde{X}$	$T^0\cdot\nu = 0;\quad \nu\cdot T^{\mathrm{PK1}} = 0$
solid-solid interfaces Σ^{SS}	$[\nu\cdot T^{\mathrm{PK1}}]^+_- = 0;\quad [T^0\cdot\nu]^+_- = 0;\quad [u]^+_- = 0$
fluid-solid interfaces Σ^{FS}	$[T^0\cdot\nu]^+_- = 0;\quad [u\cdot\nu]^+_- = 0$
& fluid-fluid interfaces Σ^{FF}	$[\nu\cdot T^{\mathrm{PK1}}]^+_- = -\nu\nabla^\Sigma\cdot(p^0[u]^+_-) - p^0 W[u]^+_-$
all interfaces Σ & $\partial\tilde{X}$	$[S(u)]^+_- = 0;\quad [\nabla S(u)\cdot\nu + 4\pi G\rho^0 u\cdot\nu]^+_- = 0$

Table 1. Boundary conditions for a general Earth model.

boundary types	linearized boundary conditions
Earth's free surface, $\partial\tilde{X}$	$T^0\cdot\nu=0;\quad \nu\cdot T^{\mathrm{L1}}=0$
solid-solid interfaces Σ^{SS}	$[\nu\cdot T^{\mathrm{L1}}]^+_-=0;\quad [T^0\cdot\nu]^+_-=0;\quad [u]^+_-=0$
fluid-solid interfaces Σ^{FS}	$[T^0\cdot\nu]^+_-=0;\quad [u\cdot\nu]^+_-=0$
& fluid-fluid interfaces Σ^{FF}	$[\nu\cdot T^{\mathrm{L1}}]^+_-=\nu[\nu\cdot T^{\mathrm{L1}}\cdot\nu]^+_-=0$
all interfaces Σ & $\partial\tilde{X}$	$[S(u)]^+_-=0;\quad [\nabla S(u)\cdot\nu+4\pi G\rho^0 u\cdot\nu]^+_-=0$

Table 2. Boundary conditions for a hydrostatic Earth model.

the incremental Lagrangian Cauchy stress. The elasticity tensor, $\Upsilon^{T^0}_{ijkl}$, attains the form,

$$\Upsilon^{T^0}_{ijkl}=c_{ijkl}+\frac{1}{2}(-T^0_{ij}\delta_{kl}+T^0_{kl}\delta_{ij}+T^0_{ik}\delta_{jl}-T^0_{jl}\delta_{ik}+T^0_{jk}\delta_{il}-T^0_{il}\delta_{jk}).$$

In fact, (4) does not determine the entire tensor T^0. It is common practice to invoke the hydrostatic assumption when $T^0_{ij}=-p^0\delta_{ij}$; then $\Upsilon^{T^0}_{ijkl}$ reduces to c_{ijkl}. With gravitational acceleration $g=-\nabla\Phi^0$, we can rewrite (5) as

$$\rho^0\omega^2 u=-\nabla\cdot(c\colon\nabla u)-\nabla(\rho^0 u\cdot g)+\nabla\cdot(\rho^0 u)g+\rho^0\nabla S(u). \tag{6}$$

In Table 2, we show the boundary conditions for system (6) assuming a hydrostatic Earth model.

2.3 The weak formulation

To study planetary normal modes, we include linear elasticity, compressible fluids, the fluid-solid and free surface boundary conditions. Discretization of the standard formulation leads to computational difficulties since the non-seismic modes from the compressible fluid pollute the computation of the point spectrum. In this paper, we restrict the solution space through a displacement-pressure while separating out the essential spectrum originating from the liquid core.

2.3.1 Choice of physical variables for fluid regions

Here, we review different approaches pertaining to the above-mentioned separation. The natural displacement formulation will result in a symmetric eigenvalue problem. However, the drawback is the existence of spurious oscillations (Kiefling & Feng 1976). Several finite-element methods have been developed for modeling the fluid regions with fluid-solid interaction: A displacement formulation (Hamdi et al. 1978), a pressure formulation (Zienkiewicz & Newton 1969; Craggs 1971), a displacement-pressure formulation (Wang & Bathe 1997), and a velocity potential formulation (Everstine 1981; Olson & Bathe 1985). However, the pressure formulation leads to a non-symmetric eigenvalue problem, see Zienkiewicz & Newton (1969); Craggs (1971); the velocity potential formulation (Everstine 1981; Olson & Bathe 1985) leads to a quadratic eigenvalue problem.

In the engineering community, several approaches have been designed to solve this issue. A penalty method (Hamdi et al. 1978) has been applied by imposing an irrotational constraint. However, the study by Olson & Bathe (1983) has shown that this penalty method has issues dealing with a solid vibrating in the fluid cavity, which is the case in this paper. A four-node element with a reduced integration with a mass matrix projection technique (Chen & Taylor 1990) has been designed to eliminate the spurious modes. A method using different elements for solid and fluid regions was proposed for two-dimensional (Bermúdez & Rodríguez 1994) and for three-dimensional cases (Bermúdez et al. 1999) while non-physical spurious modes appear (Bermúdez et al. 1995). The displacement/pressure formulation (Wang & Bathe 1997) has been developed via introducing mixed elements; still, the fluid-solid coupling needs additional consideration (Bermúdez & Rodríguez 1994; Bermúdez et al. 1999).

Compared with the above-mentioned engineering problems, we encounter a more complicated system (6) with different boundary conditions (cf. Table 2). Due to the presence of reference gravitational field and self-gravitation, the essential spectrum of the elastic-gravitational system is more complicated than that of the purely elastic systems with fluid structures in the engineering problems. In the geophysical community, the pressure formulation (Komatitsch & Tromp 2002; Nissen-Meyer et al. 2008) was used for replacing the

displacement fields in the fluid regions. It results in non-symmetric stiffness and mass matrices. Another approach used several additional variables to represent the fluid displacement (Chaljub et al. 2003, 2007), which also leads to a non-symmetric system.

To preserve the symmetry and guarantee the correct orthonormality condition for the eigenfunctions or normal modes, we must keep the fluid displacement in the formulation. In Subsection 2.3.2, we introduce a proper weak form of (6) for the hydrostatic Earth model as well as the proper relevant function spaces. We introduce an additional variable that is related to the pressure in Subsection 2.3.4 and a constraint for this new variable. We show that this new variable leads us to a symmetric system with displacements only since this new variable can later be substituted using a standard transformation. In Subsections 2.3.4 and 2.3.5, we discuss the proper formulations for both fluid and solid regions, respectively. In Subsection 2.3.3, we discuss the reason why the additional variable helps us to restrict the fluid displacement to the proper space. In Subsection 2.3.6, we restrict the computation of $S(u)$ in (2) within the computation domain. In Subsection 2.3.7, we combine all the derivations and construct our augmented weak form for numerical discretization.

2.3.2 The mass term and sesquilinear form

We let u^s denote the displacement in the solid regions and u^f denote the displacement in the fluid regions. We treat the solid and fluid parts differently and then deal with $S(u)$ globally. We use v to denote test functions and denote v^s and v^f for the solid and fluid test displacements, respectively. The mass term takes the form (with the summation convention)

$$b_H(u,v) = \int_{\Omega^{\mathrm{S}}} v_j^s u_j^s \rho^0 \,\mathrm{d}x + \int_{\Omega^{\mathrm{F}}} v_j^f u_j^f \rho^0 \,\mathrm{d}x. \tag{7}$$

We note that the original weak form of the right-hand side of (6), identified as $a_{\mathrm{original}}(u,v)$ in (de Hoop et al. 2015, (3.5)), is not coercive. In the work of de Hoop et al. (2015), a proper form, $a_2(u,v)$, for the weak formulation is introduced. The coercivity of $a_2(u,v)$ is established in (de Hoop et al. 2015, Sections 5.2 and 6). The equivalence, that is, $a_2(u,v) = a_{\mathrm{original}}(u,v)$ under the boundary conditions (cf. Table 1), is proven in (de Hoop et al. 2015, Lemma 4.1).

To set up our formulation for the numerical discretization, we start from $a_2(u,v)$. Since the original expression for $a_2(u,v)$ is derived from the first Piola-Kirchhoff stress tensor T^{PK1}, upon applying the hydrostatic assumption, integrations in $a_2(u,v)$ related to σ_N, Σ^{SS}, Σ^{FF} and $\partial\tilde{X}$ will vanish. We substitute $\tilde{s} = \nabla\rho^0 - \kappa^{-1} g(\rho^0)^2$ and then obtain

$$\begin{aligned} a_2(u,v) = &\int_{\Omega^{\mathrm{S}}} (\partial_{x_i} v_j^s)(c_{ijkl}\partial_{x_k} u_l^s)\,\mathrm{d}x + \int_{\Sigma^{\mathrm{FS}}} \mathfrak{S}\{v_j^s g_j \nu_i^{s\to f} u_i^s [\rho^0]^f\}\,\mathrm{d}\Sigma \\ &+ \int_{\Omega^{\mathrm{S}}} \mathfrak{S}\big\{(\partial_{x_j} v_j^s) g_i u_i^s \rho^0 - u_i^s (\partial_{x_i} g_j) v_j^s \rho^0 - u_i^s (\partial_{x_i} v_j^s) g_j \rho^0\big\}\,\mathrm{d}x \\ &+ \int_{\Omega^{\mathrm{F}}} \rho^0 N^2 \frac{g_j v_j^f g_i u_i^f}{\|g\|^2}\,\mathrm{d}x + \int_{\Omega^{\mathrm{F}}} \kappa(\partial_{x_j} v_j^f + \rho^0\kappa^{-1} g_j v_j^f)(\partial_{x_i} u_i^f + \rho^0\kappa^{-1} g_i u_i^f)\,\mathrm{d}x \\ &- \frac{1}{4\pi G}\int_{\mathbb{R}^3} [\partial_{x_i} S(v)][\partial_{x_i} S(u)]\,\mathrm{d}x, \end{aligned} \tag{8}$$

where κ is the bulk modulus, $N^2 = (\nabla\rho^0/\rho^0 - g\rho^0/\kappa)\cdot g$ signifies the square of the Brunt-Väisälä frequency, and $\nu^{s\to f}$ denotes the normal vector at the fluid-solid boundary pointing from the solid to the fluid side. The symmetrization operation $\mathfrak{S}$ is defined as $\mathfrak{S}\{L(u,v)\} := \frac{1}{2}(L(u,v) + L(v,u))$, for any bilinear form $L(u,v)$.

Following the work of (de Hoop et al. 2015, Definition 5.4), we introduce the space for the displacement field

$$E = \left\{ u \in L^2(\tilde{X}, \rho^0\,\mathrm{d}x) : \left\{ \begin{array}{l} u^s = u|_{\Omega^{\mathrm{S}}} \in H^1(\Omega^{\mathrm{S}}) \\ u^f = u|_{\Omega^{\mathrm{F}}} \in H(\mathrm{Div}, \Omega^{\mathrm{F}}, L^2(\partial\Omega^{\mathrm{F}})) \\ [u\cdot\nu]^+_- = 0, \text{ along } \Sigma^{\mathrm{FS}} \end{array} \right\} \right., \tag{9}$$

where

$$H(\mathrm{Div}, \Omega^{\mathrm{F}}, L^2(\partial\Omega^{\mathrm{F}})) = \{u^f \in L^2(\Omega^{\mathrm{F}}) : \nabla \cdot u^f \in L^2(\Omega^{\mathrm{F}}),\, u|_{\partial\Omega^{\mathrm{F}}} \cdot \nu \in L^2(\partial\Omega^{\mathrm{F}})\}.$$

The definitions of the other relevant function spaces can be found in (de Hoop et al. 2015, Sections 5 and 7). The solution space $H = L^2(\tilde{X}, \rho^0\,\mathrm{d}x)$ subjects to the constraint $\int_{\tilde{X}} u\rho^0\,\mathrm{d}x = 0$ removing rigid-body translations, and in which E is densely embedded, can be decomposed as (de Hoop et al. 2019)

$$H = H_1 \oplus H_2, \tag{10}$$

where space H_2 is associated with the essential spectrum. We define operator T as

$$Tu^f = \rho^0[\nabla \cdot u^f + \rho^0\kappa^{-1} g \cdot u^f]. \tag{11}$$

The adjoint, T^*, of T is given by

$$T^*\varphi = -\frac{1}{\rho^0}\nabla(\rho^0\varphi) + \rho^0\kappa^{-1} g\varphi, \tag{12}$$

where φ has the interpretation of potential. Then H_2 is defined by the constraints,

$$u^s = 0,\ Tu^f = 0 \text{ and } u^f \cdot \nu = 0 \text{ on } \Sigma^{\mathrm{FF}} \cup \Sigma^{\mathrm{FS}} \cup \partial\tilde{X}^{\mathrm{F}}.$$

In fact, u^f can be decomposed according to $\mathrm{Ran}(T^*) \oplus \mathrm{Ker}(T)$, following the decomposition according to $H_1 \oplus H_2$. In the following, we consider $a_2(u, v)$ for $u, v \in H_1$, again, to eventually compute the seismic point spectrum.

2.3.3 Restricting u^f to H_1

We will enforce that u^f lies in $\mathrm{Ran}(T^*)$ by augmenting the system of equations (cf. (8)) and introducing an additional variable, p, according to

$$-p\kappa^{-1} = \nabla \cdot u^f + \rho^0\kappa^{-1} g \cdot u^f \text{ in } \Omega^{\mathrm{F}}. \tag{13}$$

We augment the space E in (9) with the space E_p,

$$E_p = H^1(\Omega^{\mathrm{F}}). \tag{14}$$

The essence is that u^f is enforced to have the representation $u^f = T^*\varphi$ for some $\varphi \in H^1(\Omega^{\mathrm{F}})$. Here,

$$\varphi = (TT^*)^{-1}Tu^f,$$

while

$$Tu^f = -\rho^0\kappa^{-1}p.$$

Indeed, we will use p instead of φ in the process of removing any component of u^f in $\mathrm{Ker}(T)$.

Imposing the fluid-solid boundary condition $[\nu_j^{f\to s}u_j^f - \nu_j^{f\to s}u_j^s]|_{\Sigma^{\mathrm{FS}}} = 0$, we obtain the weak form for (13),

$$\begin{aligned} 0 &= \int_{\Omega^{\mathrm{F}}} v^p[-p\kappa^{-1} - \partial_{x_j}u_j^f - \rho^0\kappa^{-1}g_j u_j^f]\,\mathrm{d}x \\ &= -\int_{\Omega^{\mathrm{F}}} v^p p\kappa^{-1}\,\mathrm{d}x + \int_{\Omega^{\mathrm{F}}}[(\partial_{x_j}v^p)u_j^f - v^p g_j u_j^f \rho^0\kappa^{-1}]\,\mathrm{d}x - \int_{\Sigma^{\mathrm{FS}}} v^p\nu_j^{f\to s}u_j^s\,\mathrm{d}\Sigma \qquad (15) \\ &=: c_g([u,p], v^p) \qquad (16) \end{aligned}$$

for all $v^p \in H^1(\Omega^{\mathrm{F}})$ with $v^p|_{\partial\tilde{X}^{\mathrm{F}}} = 0$, where $\nu^{f\to s}$ denotes the normal vector at the fluid-solid boundary pointing from the fluid to the solid side. We will employ the short-hand notation, $c_g([u,p], v^p)$, in the further analysis.

2.3.4 Fluid regions

We use (13) in (8) and obtain

$$\int_{\Omega^{\mathrm{F}}} \kappa(\partial_{x_j} v_j^f + \rho^0\kappa^{-1} g_j v_j^f)(\partial_{x_i} u_i^f + \rho^0\kappa^{-1} g_i u_i^f)\,\mathrm{d}x \\ = \int_{\Omega^{\mathrm{F}}} [v_j^f(\partial_{x_j} p) - v_j^f g_j p\rho^0\kappa^{-1}]\,\mathrm{d}x - \int_{\Sigma^{\mathrm{FS}}} v_j^f \nu_j^{f\to s} p\,\mathrm{d}\Sigma. \quad (17)$$

We have

$$-\int_{\Sigma^{\mathrm{FS}}} v_j^f \nu_j^{f\to s} p\,\mathrm{d}\Sigma = \int_{\Sigma^{\mathrm{FS}}} v_j^s \nu_j^{s\to f} p\,\mathrm{d}\Sigma. \quad (18)$$

We include the right-hand side of (18) in the contributions from the solid regions. We thus obtain the contributions to $a_2(u,v)$ in (8) from the fluid regions,

$$a_2^f(u,v) = \int_{\Omega^{\mathrm{F}}} \rho^0 N^2 \frac{g_j v_j^f g_i u_i^f}{\|g\|^2}\,\mathrm{d}x + \int_{\Omega^{\mathrm{F}}} v_j^f[\partial_{x_j} p - g_j p\rho^0\kappa^{-1}]\,\mathrm{d}x, \quad (19)$$

where we identify $\nabla p - \rho^0\kappa^{-1} g p$ with $-\rho^0 T^*((\rho^0)^{-1} p)$.

2.3.5 Solid regions

For the solid regions, we include the right-hand side of (18) to the terms related to the solid regions in (8) and obtain

$$a_2^s(u,v) = \int_{\Omega^{\mathrm{S}}} (\partial_{x_i} v_j^s)(c_{ijkl}\partial_{x_k} u_l^s)\,\mathrm{d}x + \int_{\Sigma^{\mathrm{FS}}} \mathfrak{S}\{v_j^s g_j \nu_i^{s\to f} u_i^s [\rho^0]^f\}\,\mathrm{d}\Sigma \\ + \int_{\Sigma^{\mathrm{FS}}} v_j^s \nu_j^{s\to f} p\,\mathrm{d}\Sigma + \int_{\Omega^{\mathrm{S}}} \mathfrak{S}\{(\partial_{x_j} v_j^s) g_i u_i^s \rho^0 - \rho^0 u_i^s (\partial_{x_i} g_j) v_j^s - \rho^0 u_i^s (\partial_{x_i} v_j^s) g_j\}\,\mathrm{d}x. \quad (20)$$

Combining (16), (19) and (20) we obtain a complex symmetric bilinear form for a non-rotating hydrostatic planet, not including the incremental gravitational terms.

2.3.6 Incremental gravitational potential

Here, we discuss the contribution of the perturbation of the gravitational potential $S(u)$,

$$-\frac{1}{4\pi G}\int_{\mathbb{R}^3} [\partial_{x_i} S(v)][\partial_{x_i} S(u)]\,\mathrm{d}x = \int_{\tilde{X}} v_i[\partial_{x_i} S(u)]\rho^0\,\mathrm{d}x \quad (21)$$

Since we decompose the test functions into test functions on solid and fluid regions, we rewrite (21) as

$$\int_{\tilde{X}} v_i[\partial_{x_i} S(u)]\rho^0\,\mathrm{d}x = \int_{\Omega^{\mathrm{S}}} v_i^s[\partial_{x_i} S(u)]\rho^0\,\mathrm{d}x + \int_{\Omega^{\mathrm{F}}} v_i^f[\partial_{x_i} S(u)]\rho^0\,\mathrm{d}x = \\ -\int_{\Omega^{\mathrm{S}}} [\partial_{x_i}(\rho^0 v_i^s)] S(u)\,\mathrm{d}x - \int_{\Sigma^{\mathrm{SS}}\cup\partial\tilde{X}^{\mathrm{S}}} \nu_i v_i^s S(u)[\rho^0]_-^+\,\mathrm{d}\Sigma - \int_{\Sigma^{\mathrm{FS}}} \nu_i^{f\to s} v_i^s S(u)[\rho^0]^s\,\mathrm{d}\Sigma \\ -\int_{\Omega^{\mathrm{F}}} [\partial_{x_i}(\rho^0 v_i^f)] S(u)\,\mathrm{d}x - \int_{\Sigma^{\mathrm{FF}}\cup\partial\tilde{X}^{\mathrm{F}}} \nu_i v_i^f S(u)[\rho^0]_-^+\,\mathrm{d}\Sigma - \int_{\Sigma^{\mathrm{FS}}} \nu_i^{s\to f} v_i^f S(u)[\rho^0]^f\,\mathrm{d}\Sigma, \quad (22)$$

where $[\rho^0]^s$ denotes the solid density along the fluid-solid boundary. One can set up $S(u)$ as an independent variable and apply the finite-infinite element method to approximate (2), but here we follow a different approach.

Making use of the Green's function (Dahlen & Tromp 1998, Chapter 3, (3.98)), we have

$$S(u) = G\int_{\tilde{X}} \frac{\nabla'\cdot(\rho^0(x')u(x'))}{\|x-x'\|}\,\mathrm{d}x' + G\int_{\Sigma\cup\partial\tilde{X}} \frac{\nu(x')\cdot u(x')[\rho^0(x')]_-^+}{\|x-x'\|}\,\mathrm{d}\Sigma'. \quad (23)$$

Again, we separate the displacement field u into u^s and u^f, and rewrite (23) as

$$\begin{aligned}S(u) = G\int_{\Omega^{\mathrm{S}}} \frac{\nabla'\cdot(\rho^0(x')u^s(x'))}{\|x-x'\|}\,\mathrm{d}x' + G\int_{\Omega^{\mathrm{F}}} \frac{\nabla'\cdot(\rho^0(x')u^f(x'))}{\|x-x'\|}\,\mathrm{d}x' \\ + G\int_{\Sigma^{\mathrm{SS}}\cup\partial\tilde{X}^{\mathrm{S}}} \frac{\nu(x')\cdot u^s(x')[\rho^0(x')]^+_-}{\|x-x'\|}\,\mathrm{d}\Sigma' + G\int_{\Sigma^{\mathrm{FS}}} \frac{[\rho^0(x')]^s\nu^{f\to s}(x')\cdot u^s(x')}{\|x-x'\|}\,\mathrm{d}\Sigma' \\ + G\int_{\Sigma^{\mathrm{FF}}\cup\partial\tilde{X}^{\mathrm{F}}} \frac{\nu(x')\cdot u^f(x')[\rho^0(x')]^+_-}{\|x-x'\|}\,\mathrm{d}\Sigma' + G\int_{\Sigma^{\mathrm{FS}}} \frac{[\rho^0(x')]^f\nu^{s\to f}(x')\cdot u^f(x')}{\|x-x'\|}\,\mathrm{d}\Sigma'. \end{aligned} \tag{24}$$

Although we impose $\nu^{s\to f}\cdot u^f = \nu^{s\to f}\cdot u^s$ along the fluid-solid boundaries, we keep the construction of the incremental gravitational potential $S(u)$ as described in (24). This is to preserve the symmetry of the bilinear form as we substitute (24) into (22).

Since the fundamental solution is known, we apply the FMM to evaluate $S(u)$ for a given displacement u via (24). Utilization of this approach is computationally attractive but requires that the eigensolver can solve for the interior eigenmodes via matrix-vector multiplications.

2.3.7 Summary

We combine the weak formulations in fluid and solid regions (19), (20), the constraint in the fluid regions (16) and the perturbation of the gravitational potential (21) in rewriting $a_2(u,v)$ in (8)

$$\begin{aligned}a_2([u,p,S(u)],v) = \int_{\Omega^{\mathrm{S}}} (\partial_{x_i}v_j^s)(c_{ijkl}\partial_{x_k}u_l^s)\,\mathrm{d}x + \int_{\Sigma^{\mathrm{FS}}} \mathfrak{S}\{v_j^s g_j \nu_i^{s\to f} u_i^s [\rho^0]^f\}\,\mathrm{d}\Sigma \\ + \int_{\Sigma^{\mathrm{FS}}} v_j^s\nu_j^{s\to f} p\,\mathrm{d}\Sigma + \int_{\Omega^{\mathrm{S}}} \mathfrak{S}\{(\partial_{x_j}v_j^s)g_i u_i^s\rho^0 - u_i^s(\partial_{x_i}g_j)v_j^s\rho^0 - u_i^s(\partial_{x_i}v_j^s)g_j\rho^0\}\,\mathrm{d}x \\ + \int_{\Omega^{\mathrm{F}}} \rho^0 N^2 \frac{g_j v_j^f g_i u_i^f}{\|g\|^2}\,\mathrm{d}x + \int_{\Omega^{\mathrm{F}}} v_j^f[\partial_{x_j}p - g_j p\rho^0\kappa^{-1}]\,\mathrm{d}x - \frac{1}{4\pi G}\int_{\mathbb{R}^3}[\partial_{x_i}S(v)][\partial_{x_i}S(u)]\,\mathrm{d}x. \end{aligned} \tag{25}$$

To restrict the domain of integration in the term $(4\pi G)^{-1}\int_{\mathbb{R}^3}[\partial_{x_i}S(v)][\partial_{x_i}S(u)]\,\mathrm{d}x$ in (25) to the computational domain, we use relation (21) and obtain

$$\begin{aligned}a_2([u,p,S(u)],v) = \int_{\Omega^{\mathrm{S}}} (\partial_{x_i}v_j^s)(c_{ijkl}\partial_{x_k}u_l^s)\,\mathrm{d}x + \int_{\Sigma^{\mathrm{FS}}} \mathfrak{S}\{v_j^s g_j \nu_i^{s\to f} u_i^s [\rho^0]^f\}\,\mathrm{d}\Sigma \\ + \int_{\Sigma^{\mathrm{FS}}} v_j^s\nu_j^{s\to f} p\,\mathrm{d}\Sigma + \int_{\Omega^{\mathrm{S}}} \mathfrak{S}\{(\partial_{x_j}v_j^s)g_i u_i^s\rho^0 - u_i^s(\partial_{x_i}g_j)v_j^s\rho^0 - u_i^s(\partial_{x_i}v_j^s)g_j\rho^0\}\,\mathrm{d}x \\ - \int_{\Omega^{\mathrm{S}}} [\partial_{x_i}(\rho^0 v_i^s)]S(u)\,\mathrm{d}x - \int_{\Sigma^{\mathrm{SS}}\cup\partial\tilde{X}^{\mathrm{S}}} \nu_i v_i^s S(u)[\rho^0]^+_-\,\mathrm{d}\Sigma - \int_{\Sigma^{\mathrm{FS}}} \nu_i^{f\to s} v_i^s S(u)[\rho^0]^s\,\mathrm{d}\Sigma \\ + \int_{\Omega^{\mathrm{F}}} \rho^0 N^2 \frac{g_j v_j^f g_i u_i^f}{\|g\|^2}\,\mathrm{d}x + \int_{\Omega^{\mathrm{F}}} v_j^f[\partial_{x_j}p - g_j p\rho^0\kappa^{-1}]\,\mathrm{d}x \\ - \int_{\Omega^{\mathrm{F}}} [\partial_{x_i}(\rho^0 v_i^f)]S(u)\,\mathrm{d}x - \int_{\Sigma^{\mathrm{FF}}\cup\partial\tilde{X}^{\mathrm{F}}} \nu_i v_i^f S(u)[\rho^0]^+_-\,\mathrm{d}\Sigma - \int_{\Sigma^{\mathrm{FS}}} \nu_i^{s\to f} v_i^f S(u)[\rho^0]^f\,\mathrm{d}\Sigma. \end{aligned} \tag{26}$$

We find the complete linear system from (7), (26) and constraint (16):

$$\begin{cases} a_2([u,p,S(u)],v) & = \omega^2 b_H(u,v), \\ c_g([u,p],v^p) & = 0, \end{cases} \tag{27}$$

where $S(u)$ satisfies (24).

We will evaluate the normal modes of the A_{11} component in the space H_1 (de Hoop et al. 2019) via solving (27) and obtain the seismic point spectrum, strictly asymptotically. In the presence of an essential spectrum with $N^2 \neq 0$, the normal mode summation (that is, the resolution of the identity) is not exact and holds asymptotically correct.

We note that $b_H/2$ in (7) and $a_2/2$ in (26) correspond with the kinetic and elastic-gravitational energies, respectively. Combining these and using $p(u^f, u^s|_{\Sigma^{\mathrm{FS}}})$ in (26) as the solution of (16), we obtain the action $\mathcal{L}$ of our proposed system (Dahlen & Tromp 1998, (4.26))

$$\mathcal{L} = \frac{1}{2}\left(\omega^2 b_H(u,u) - a_2([u,p(u^f,u^s|_{\Sigma^{\mathrm{FS}}}),S(u)],u)\right). \tag{28}$$

In the Cowling approximation, one replaces a_2 by a_C, where

$$a_C([u,p],v) = a_2([u,p,S(u)],v) + \frac{1}{4\pi G}\int_{\mathbb{R}^3}[\partial_{x_i}S(v)][\partial_{x_i}S(u)]\,\mathrm{d}x. \tag{29}$$

where a_C denotes the weak form for the so-called Cowling approximation. Then

$$\begin{cases} a_C([u,p],v) & = \omega^2 b_H(u,v), \\ c_g([u,p],v^p) & = 0. \end{cases} \tag{30}$$

We first consider the Cowling approximation, in Section 3, while introducing the mixed FEM. We then add the incremental gravitational potential in Section 4, while introducing the FMM leading to a discretization of (27).

3 THE CONTINUOUS GALERKIN MIXED FINITE-ELEMENT METHOD

In this section, we employ the Continuous Galerkin mixed finite-element method, see Zienkiewicz & Taylor (2005); Bathe (2006); Hughes (2012); Brezzi & Fortin (2012); Ern & Guermond (2013), for discretizing our system (30) assuming the Cowling approximation. We thus obtain a matrix representation for (30). The incremental gravitational potential will be introduced in the discretization in Subsection 4.2.

3.1 The Continuous Galerkin mixed finite-element approximation

Given a shape regular finite-element partitioning $\mathcal{T}_h$ of the domain $\tilde{X}$, we denote an element of the mesh by $K_k \in \mathcal{T}_h$ and a boundary element by $E_l \subset \partial K_k$ and have

$$\tilde{X} \approx \bigcup_{k=1}^{N_K} K_k, \quad \Sigma \cup \partial\tilde{X} \approx \bigcup_{l=1}^{N_E} E_l \subseteq \bigcup_{k=1}^{N_K} \partial K_k,$$

where N_K denotes the total number of volume elements and N_E denotes the total number of interior and exterior boundary elements. Furthermore, we let K_k^{S} and K_k^{F} be elements in the solid and fluid regions, respectively. Similarly, E_l^{S}, E_l^{F} and E_l^{FS} denote boundary elements on the solid $\Sigma^{\mathrm{SS}} \cup \partial\tilde{X}^{\mathrm{S}}$, fluid $\Sigma^{\mathrm{FF}} \cup \partial\tilde{X}^{\mathrm{F}}$ and fluid-solid Σ^{FS} discontinuities, respectively. We have

$$\begin{aligned} \Omega^{\mathrm{S}} &\approx \bigcup_{k=1}^{N_K^{\mathrm{S}}} K_k^{\mathrm{S}}, \quad \Omega^{\mathrm{F}} \approx \bigcup_{k=1}^{N_K^{\mathrm{F}}} K_k^{\mathrm{F}}, \\ \Sigma^{\mathrm{FS}} &\approx \bigcup_{l=1}^{N_E^{\mathrm{FS}}} E_l^{\mathrm{FS}}, \quad \Sigma^{\mathrm{SS}} \cup \partial\tilde{X}^{\mathrm{S}} \approx \bigcup_{l=1}^{N_E^{\mathrm{S}}} E_l^{\mathrm{S}}, \quad \Sigma^{\mathrm{FF}} \cup \partial\tilde{X}^{\mathrm{F}} \approx \bigcup_{l=1}^{N_E^{\mathrm{F}}} E_l^{\mathrm{F}} \end{aligned}$$

with

$$N_K = N_K^{\mathrm{S}} + N_K^{\mathrm{F}}, \quad N_E = N_E^{\mathrm{S}} + N_E^{\mathrm{F}} + N_E^{\mathrm{FS}},$$

where N_K^{S} and N_K^{F} denote the total number of volume elements in the solid and fluid regions, respectively, and N_E^{S}, N_E^{F} and N_E^{FS} denote the total number of boundary elements on the (interior/exterior) solid, fluid and fluid-solid boundaries, respectively. In the above, h signifies the maximum value of diameters of all the elements.

Since we separate out the fluid and solid regions, we divide the finite-element partitioning accordingly into

$$\mathcal{T}_h = \mathcal{T}_h^{\mathrm{S}} + \mathcal{T}_h^{\mathrm{F}}, \quad \Sigma_h^{\mathrm{FS}} = \mathcal{T}_h^{\mathrm{S}} \cap \mathcal{T}_h^{\mathrm{F}},$$

where $\mathcal{T}_h^{\mathrm{S}}$, $\mathcal{T}_h^{\mathrm{F}}$ and Σ_h^{FS} denote the partitioning of the domain Ω^{S}, Ω^{F} and Σ^{FS}, respectively. We then introduce E_h as the finite-element space corresponding with E in (9),

$$E_h = \left\{ u_h : \left\{ \begin{array}{l} u_h^s \in \mathbf{V}_h^s := \left\{ v_h^s \in H^1(\Omega^{\mathrm{S}}) : v_h^s|_K \in \mathcal{P}_{p^s}(K),\ K \in \mathcal{T}_h^{\mathrm{S}} \right\}, \\ u_h^f \in \mathbf{V}_h^f := \left\{ v_h^f \in H(\mathrm{Div}, \Omega^{\mathrm{F}}, L^2(\partial\Omega^{\mathrm{F}}) : v_h^f|_K \in \mathcal{P}_{p^f}(K),\ K \in \mathcal{T}_h^{\mathrm{F}} \right\}, \\ \displaystyle\int_{E^{\mathrm{FS}}} [u_h \cdot \nu]_-^+ v_h^p \,\mathrm{d}\Sigma = 0 \text{ for all } E^{\mathrm{FS}} \subset \Sigma_h^{\mathrm{FS}} \end{array} \right. \right\} \tag{31}$$

and $\mathbf{V}_h^p$ as the finite-element space for p,

$$\mathbf{V}_h^p := \left\{ v_h^p \in H^1(\Omega^{\mathrm{F}}) : v_h^p|_K \in \mathcal{P}_{p^p}(K),\ K \in \mathcal{T}_h^{\mathrm{F}} \right\}.$$

Here, $\mathcal{P}_{p^s}(K)$ and $\mathcal{P}_{p^f}(K)$ are the spaces of polynomials of degrees p^s and p^f, respectively; $\mathcal{P}_{p^p}(K)$ is the space of polynomials of degree p^p. By the Galerkin method, the finite-element solutions, u_h, and test functions, v_h, both lie in E_h and $\mathbf{V}_h^p$. We note that the polynomial degree p^p does not need to be equal to p^f.

We apply non-conforming finite elements across fluid-solid boundaries. The fluid-solid transmission condition in the definition of E has been replaced by the condition $\int_{E^{\mathrm{FS}}} [u_h \cdot \nu]_-^+ v_h^p \,\mathrm{d}\Sigma = 0$ in the definition of E_h. The fluid-solid transmission condition holds in the form of a boundary integration. For low-degree polyomials we show, in the next subsection, that these conditions are compatible through our formulation. Such a compatibility was analyzed and discussed by Bermúdez & Rodríguez (1994); Bermúdez et al. (1995); Brezzi & Fortin (2012). Several numerical studies (Kiefling & Feng 1976; Zienkiewicz & Bettess 1978; Olson & Bathe 1985; Chen & Taylor 1990; Bermúdez et al. 1999) have been performed using similar non-conforming schemes along the fluid-solid boundaries. For the general theory and analysis of the mixed FEM, we refer to Brezzi & Fortin (2012).

3.2 Fluid-solid transmission condition

Here, we discuss the realization of the fluid-solid transmission condition using the mixed FEM. In a_2 of (26), we utilize the additional variable p to impose continuity of the normal stress across the fluid-solid boundaries.

We insert any v_h^p in Ω^{F} with $v_h^p|_{\Sigma_h^{\mathrm{FS}}} = 0$ to in the system (30) and then evaluate the integration over all the elements and obtain

$$\begin{aligned} 0 &= \sum_{k=1}^{N_K^{\mathrm{F}}} \int_{K_k^{\mathrm{F}}} \Big[- v_h^p p_h \kappa^{-1} + (\nabla \cdot v_h^p) u_h^f - v_h^p (g \cdot u_h^f) \rho^0 \kappa^{-1} \Big] \,\mathrm{d}x \\ &= \sum_{k=1}^{N_K^{\mathrm{F}}} \int_{K_k^{\mathrm{F}}} v_h^p \Big[- \kappa^{-1} p_h - \nabla \cdot u_h^f - \rho^0 \kappa^{-1} (g \cdot u_h^f) \Big] \,\mathrm{d}x \qquad \forall v_h^p \text{ with } v_h^p|_{\Sigma_h^{\mathrm{FS}}} = 0, \end{aligned}$$

Since the above equation holds for any basis with $v_h^p|_{\Sigma_h^{\mathrm{FS}}} = 0$, constraint (13) is then satisfied in the integral over each element. We then insert any basis element for v_h^p with $v_h^p|_{\Sigma_h^{\mathrm{FS}}} \neq 0$ in system (30) and obtain

$$\begin{aligned} 0 &= \sum_{k=1}^{N_K^{\mathrm{F}}} \int_{K_k^{\mathrm{F}}} \Big[- v_h^p p_h \kappa^{-1} + (\nabla \cdot v_h^p) u_h^f - v_h^p (g \cdot u_h^f) \rho^0 \kappa^{-1} \Big] \,\mathrm{d}x + \sum_{l=1}^{N_E^{\mathrm{F}}} \int_{E_l^{\mathrm{FS}}} - v_h^p (\nu^{f\to s} \cdot u_h^s) \,\mathrm{d}\Sigma \\ &= \sum_{k=1}^{N_K^{\mathrm{F}}} \int_{K_k^{\mathrm{F}}} v_h^p \Big[- \kappa^{-1} p_h - \nabla \cdot u_h^f - \rho^0 \kappa^{-1} (g \cdot u_h^f) \Big] \,\mathrm{d}x + \sum_{l=1}^{N_E^{\mathrm{F}}} \int_{E_l^{\mathrm{FS}}} v_h^p (\nu^{f\to s} \cdot u_h^f - \nu^{f\to s} \cdot u_h^s) \,\mathrm{d}\Sigma \\ &= \sum_{l=1}^{N_E^{\mathrm{F}}} \int_{E_l^{\mathrm{FS}}} v_h^p (\nu^{f\to s} \cdot u_h^f - \nu^{f\to s} \cdot u_h^s) \,\mathrm{d}\Sigma \qquad \forall v_h^p \text{ with } v_h^p|_{\Sigma_h^{\mathrm{FS}}} \neq 0. \end{aligned}$$

We probe this equation with a local basis that is non-vanishing on elements indexed by $k_1, \ldots, k_4$ as illustrated in Fig. 3. For simplicity of explanation, we choose a description in 2D in Fig. 3. We obtain the integration over boundary elements indexed by l_1 and l_2,

$$\int_{E_{l_1}^{\mathrm{FS}} \cup E_{l_2}^{\mathrm{FS}}} v_h^p (\nu^{f\to s} \cdot u_h^f - \nu^{f\to s} \cdot u_h^s) \,\mathrm{d}\Sigma = 0.$$

Similarly, if we apply a local basis that is non-vanishing on elements indexed by k_4 and k_5, we obtain the integration over boundary elements indexed by l_2 and l_3,

$$\int_{E_{l_2}^{\mathrm{FS}} \cup E_{l_3}^{\mathrm{FS}}} v_h^p (\nu^{f\to s} \cdot u_h^f - \nu^{f\to s} \cdot u_h^s) \,\mathrm{d}\Sigma = 0.$$

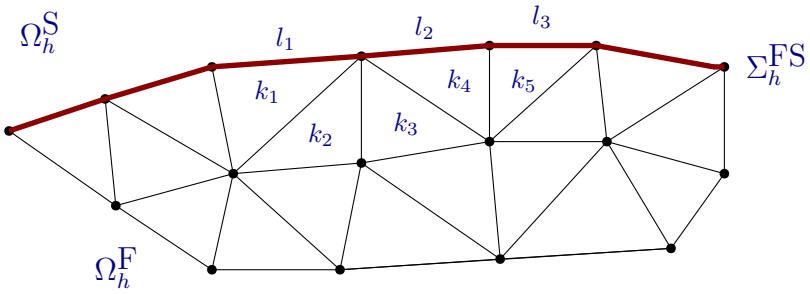

Figure 3. Illustration of the partition on the fluid-solid boundary. Elements k_1 – k_5 and boundary elements l_1 – l_3 are marked.

It is apparent that

$$\int_{E_{l_1}^{\mathrm{FS}}} v_h^p(\nu^{f\to s}\cdot u_h^f-\nu^{f\to s}\cdot u_h^s)\,\mathrm{d}\Sigma=\int_{E_{l_3}^{\mathrm{FS}}} v_h^p(\nu^{f\to s}\cdot u_h^f-\nu^{f\to s}\cdot u_h^s)\,\mathrm{d}\Sigma=0\qquad\forall\, E_{l_1}^{\mathrm{FS}}\in\Sigma_h^{\mathrm{FS}}.$$

Thus, the non-conforming scheme converges on the barycenters of the boundary elements if low-order polynomials are utilized as local basis functions for the fluid regions and fluid-solid boundaries (Bermúdez et al. 1995, 1999).

3.3 Matrix formulae

We use mixed finite-element bases to build up each submatrix derived from (30). We introduce nodal based Lagrange polynomials, $\{\ell_i^s\}$, $\{\ell_i^f\}$, $\{\ell_i^p\}$, on the respective volume elements $K\in\mathcal{T}_h^{\mathrm{S}}$, $\mathcal{T}_h^{\mathrm{F}}$. We set $N_{p^s}=(p^s+1)(p^s+2)(p^s+3)/6$, where N_{p^s} is the number of nodes on a tetrahedron for the p^s-th order

operations	physical relations	corresponding formulae
$(\tilde{v}^s)^{\mathsf{T}}A_{sg}\tilde{u}^s$	solid stiffness matrix with g	$\int_{\Omega^{\mathrm{S}}}\nabla v_h^s:(c:\nabla u_h^s)\,\mathrm{d}x$ $+\int_{\Sigma^{\mathrm{FS}}}\mathfrak{S}\Big\{(v_h^s\cdot g)(\nu^{s\to f}\cdot u_h^s)[\rho^0]^f\Big\}\,\mathrm{d}\Sigma$ $+\int_{\Omega^{\mathrm{S}}}\mathfrak{S}\Big\{(\nabla\cdot v_h^s)(g\cdot u_h^s)\rho^0$ $-u_h^s\cdot(\nabla g)\cdot v_h^s\rho^0-u_h^s\cdot(\nabla v_h^s)\cdot g\rho^0\Big\}\,\mathrm{d}x$
$(\tilde{v}^f)^{\mathsf{T}}A_f\tilde{u}^s$	Brunt-Väisälä frequency	$\int_{\Omega^{\mathrm{F}}}\rho^0N^2\frac{(g\cdot v_h^f)(g\cdot u_h^f)}{\|g\|^2}\,\mathrm{d}x$
$(\tilde{v}^p)^{\mathsf{T}}A_p\tilde{p}$	fluid potential	$\int_{\Omega^{\mathrm{F}}}-v_h^pp_h\kappa^{-1}\,\mathrm{d}x$
$(\tilde{v}^f)^{\mathsf{T}}A_{\mathrm{dg}}\tilde{p}$	fluid stiffness matrix with g	$\int_{\Omega^{\mathrm{F}}}v_h^f\cdot\left[(\nabla p_h)-gp_h\rho^0\kappa^{-1}\right]\,\mathrm{d}x$
$(\tilde{v}^p)^{\mathsf{T}}A_{\mathrm{dg}}^{\mathsf{T}}\tilde{u}^f$	constraint with g	$\int_{\Omega^{\mathrm{F}}}\left[\nabla v_h^p\cdot u_h^f-v_h^p(g\cdot u_h^f)\rho^0\kappa^{-1}\right]\,\mathrm{d}x$
$(\tilde{v}^s)^{\mathsf{T}}E_{\mathrm{FS}}\tilde{p}$	fluid-solid boundary condition	$\int_{\Sigma^{\mathrm{FS}}}(v_h^s\cdot\nu^{s\to f})p_h\,\mathrm{d}\Sigma$
$(\tilde{v}^p)^{\mathsf{T}}E_{\mathrm{FS}}^{\mathsf{T}}\tilde{u}^f$	fluid-solid boundary condition	$\int_{\Sigma^{\mathrm{FS}}}-v_h^p(\nu^{f\to s}\cdot u_h^s)\,\mathrm{d}\Sigma$
$(\tilde{v}^s)^{\mathsf{T}}M_s\tilde{u}^s$	solid mass matrix	$\int_{\Omega^{\mathrm{S}}}v_h^s\cdot u_h^s\rho^0\,\mathrm{d}x$
$(\tilde{v}^f)^{\mathsf{T}}M_f\tilde{u}^f$	fluid mass matrix	$\int_{\Omega^{\mathrm{F}}}v_h^f\cdot u_h^f\rho^0\,\mathrm{d}x$

Table 3. Implicit definition of the matrices for the Cowling approximation. In the above, $\int_{\Omega^{\mathrm{S}}}=\sum_{k=1}^{N_K^{\mathrm{S}}}\int_{K_k^{\mathrm{S}}}$, $\int_{\Omega^{\mathrm{F}}}=\sum_{k=1}^{N_K^{\mathrm{F}}}\int_{K_k^{\mathrm{F}}}$ and $\int_{\Sigma^{\mathrm{FS}}}=\sum_{l=1}^{N_E^{\mathrm{FS}}}\int_{E_l^{\mathrm{FS}}}$.

polynomial approximation. We have likewise expressions for N_{p^f} and N_{p^p}. We write

$$(u_h^s)_j(x) = \sum_{i=1}^{N_{p^s}} (u_h^s)_j(x_i)\ell_i^s(x), \tag{32}$$

$$(u_h^f)_j(x) = \sum_{i=1}^{N_{p^f}} (u_h^f)_j(x_i)\ell_i^f(x), \tag{33}$$

$$p_h(x) = \sum_{i=1}^{N_{p^p}} p(x_i)\ell_i^p(x), \tag{34}$$

for $x \in K$; similar representations hold for v_h^s, v_h^f, v_h^p, respectively. We collect the values of u_h^s, u_h^f, p_h and v_h^s, v_h^f, v_h^p at all the nodes, $\{x_i\}$, in the vectors $\tilde{u}^s$, $\tilde{u}^f$, $\tilde{p}$ and $\tilde{v}^s$, $\tilde{v}^f$, $\tilde{v}^p$, respectively. We then assemble local matrices that represent the discretized system with respect to the mentioned Lagrange polynomials following Table 3. We obtain

$$\begin{pmatrix} A_{sg} & 0 & E_{\mathrm{FS}} \\ 0 & A_f & A_{\mathrm{dg}} \\ E_{\mathrm{FS}}^{\mathsf{T}} & A_{\mathrm{dg}}^{\mathsf{T}} & A_p \end{pmatrix} \begin{pmatrix} \tilde{u}^s \\ \tilde{u}^f \\ \tilde{p} \end{pmatrix} = \omega^2 \begin{pmatrix} M_s & 0 & 0 \\ 0 & M_f & 0 \\ 0 & 0 & 0 \end{pmatrix} \begin{pmatrix} \tilde{u}^s \\ \tilde{u}^f \\ \tilde{p} \end{pmatrix}. \tag{35}$$

We introduce submatrices

$$A_G = \begin{pmatrix} A_{sg} & 0 \\ 0 & A_f \end{pmatrix},\ E_G = \begin{pmatrix} E_{\mathrm{FS}} \\ A_{\mathrm{dg}} \end{pmatrix},\ M = \begin{pmatrix} M_s & 0 \\ 0 & M_f \end{pmatrix}$$

and write

$$\tilde{u} = \begin{pmatrix} \tilde{u}^s \\ \tilde{u}^f \end{pmatrix}.$$

In fact, matrices A_G, A_p, E_G, and M are sparse. Because A_p is symmetric positive definite, we can substitute $\tilde{p} = -A_p^{-1}E_G^{\mathsf{T}}\tilde{u}$ in (35) and obtain

$$(A_G - E_G A_p^{-1} E_G^{\mathsf{T}})\tilde{u} = \omega^2 M\tilde{u}. \tag{36}$$

If the planet does not contain fluid regions, we can simplify (36) to

$$A_{sg}\tilde{u}^s = \omega^2 M_s \tilde{u}^s. \tag{37}$$

3.4 Construction of orthonormal bases and local matrices

Here, we introduce three-dimensional polynomial bases $\{\psi_n^s\}_{n=1}^{N_{p^s}}$, $\{\psi_n^f\}_{n=1}^{N_{p^f}}$ and $\{\psi_n^p\}_{n=1}^{N_{p^p}}$ while addressing the fact that the Lagrange polynomials are not orthogonal to one another. We suppress superscripts s, f, p in the notation in the remainder of this subsection. To simplify the computations, we introduce reference volume and boundary elements. That is, we introduce a mapping that connects any element K to the reference tetrahedron defined by

$$\mathbf{I} = \{r = (r_1, r_2, r_3)\ :\ r_1 \geq -1,\ r_2 \geq -1,\ r_3 \geq -1,\ r_1 + r_2 + r_3 \leq -1\}.$$

Likewise, we introduce a mapping that connects any boundary element E to the reference triangle is defined by

$$\mathbf{I}_{2D} = \{t = (t_1, t_2)\ :\ t_1 \geq -1,\ t_2 \geq -1,\ t_1 + t_2 \leq 0\}.$$

We note that any two tetrahedra are connected through an affine transformation, $x \to r$, with a constant Jacobian, J say, which is the determinant of $(\partial_r x)$. For the local approximation on the reference element $\mathbf{I}$, we have

$$u_j(r) = \sum_{n=1}^{N_p} (\hat{u}_j)_n \psi_n(r) = \sum_{i=1}^{N_p} u_j(r_i)\ell_i(r).$$

The vector fields are treated component-wise in our discretization. This yields the expression $\mathcal{V}\hat{u}_j = u_j$, where the generalized Vandermonde matrix takes the form of $\mathcal{V}_{in} = \psi_n(r_i)$ with i, n as indices of nodal

points. Here, $\{\psi_n\}$ is a polynomial basis that is orthonormal on $\mathbf{I}$. We later introduce submatrices of $\mathcal{V}$. We then evaluate derivatives and mass matrices according to

$$\partial_{x_i} = (\partial_{x_i} r_j)\mathcal{D}_j, \quad \mathcal{D}_j = (\partial_{r_j}\mathcal{V})\mathcal{V}^{-1}, \quad \mathcal{M} = \mathcal{V}^{-T}\mathcal{V}^{-1},$$

where $\mathcal{D}_j$ and $\mathcal{M}$ are the derivative matrix and the mass matrix on the reference tetrahedron. More details of the constructions of J, $\mathcal{V}$, $\mathcal{D}_j$ and $\mathcal{M}$ can be found in (Hesthaven & Warburton 2007, Chapter 10.1). Thus, we introduce

$$\mathcal{V}_s,\ \mathcal{V}_f,\ \mathcal{V}_p, \quad \mathcal{M}_s,\ \mathcal{M}_f,\ \mathcal{M}_p \quad \text{and} \quad \mathcal{D}_j^s,\ \mathcal{D}_j^f,\ \mathcal{D}_j^p.$$

We employ the notation

$$\mathsf{D}_i^s = (\partial_{x_i} r_j)\mathcal{D}_j^s, \quad \mathsf{D}_i^f = (\partial_{x_i} r_j)\mathcal{D}_j^f, \quad \mathsf{D}_i^p = (\partial_{x_i} r_j)\mathcal{D}_j^p,$$

reflecting the mapping of the derivatives from the reference tetrahedron to the target element. We follow a likewise approach for boundary elements and introduce

$$\mathcal{M}_s^{2D},\ \mathcal{M}_f^{2D} \quad \text{and} \quad J^{2D},$$

where $\mathcal{M}_s^{2D}$ and $\mathcal{M}_f^{2D}$ are the mass matrices for solid and fluid boundary elements, respectively; J^{2D} denotes the Jacobian, which is the determinant of $(\partial_t x)$ on the boundary element. The construction of the mass matrices $\mathcal{M}_s^{2D}$ and $\mathcal{M}_f^{2D}$ on the reference triangle $\mathbf{I}_{2D}$ is similar to the one of $\mathcal{M}$ (Hesthaven & Warburton 2007, Chapter 6.1).

3.4.1 Local matrices: A_{sg}, A_f, A_p, M_s and M_f

We extract $\tilde{u}^s|_{K_k}$, $\tilde{u}^f|_{K_k}$ and $\tilde{p}|_{K_k}$ from $\tilde{u}^s$, $\tilde{u}^f$ and $\tilde{p}$, respectively, by restricting the nodes to the ones of element K_k. In a smimilar fashion, we extract $\tilde{v}^s|_{K_k}$, $\tilde{v}^f|_{K_k}$ and $\tilde{v}^p|_{K_k}$ on any element K_k. For the evaluation of matrix A_{sg} in Table 3 we need to evaluate the local matrices on element K_k through

$$\int_{K_k^{\mathrm{S}}} \partial_{x_i}(v_h^s)_j (c_{ijmn}\partial_{x_m}(u_h^s)_n)\,\mathrm{d}x = (\tilde{v}_j^s|_{K_k})^T [J_k(\mathsf{D}_i^s)^{\mathsf{T}} c_{ijmn}^k \mathcal{M}_s \mathsf{D}_m^s]\tilde{u}_n^s|_{K_k}, \tag{38}$$

$$\int_{K_k^{\mathrm{S}}} \partial_{x_i}(v_h^s)_i g_j (u_h^s)_j \rho^0\,\mathrm{d}x = (\tilde{v}_i^s|_{K_k})^T [J_k(\mathsf{D}_i^s)^{\mathsf{T}} \rho_k^0 \mathcal{M}_s D_{g_j}]\tilde{u}_j^s|_{K_k}, \tag{39}$$

$$\int_{K_k^{\mathrm{S}}} -(u_h^s)_i \partial_{x_i} g_j (v_h^s)_j \rho^0\,\mathrm{d}x = (\tilde{v}_i^s|_{K_k})^T [-J_k \rho_k^0 D_{\partial_{x_i} g_j} \mathcal{M}_s]\tilde{u}_j^s|_{K_k}, \tag{40}$$

$$\int_{K_k^{\mathrm{S}}} -(u_h^s)_j (\partial_{x_j}(v_h^s)_i) g_i \rho^0\,\mathrm{d}x = (\tilde{v}_i^s|_{K_k})^T [-J_k \mathsf{D}_j^s \mathcal{M}_s \rho_k^0 D_{g_i}]\tilde{u}_j^s|_{K_k}, \tag{41}$$

where c_{ijmn}^k, ρ_k^0 and J_k denote the stiffness tensor, density and Jacobian on element K_k, respectively; D_{g_i} and $D_{\partial_{x_i} g_j}$ denote the diagonal matrices whose diagonal entries are g_i and $\partial_{x_i} g_j$, respectively. For the evaluation of the boundary integration in A_{sg}, we need to evaluate the local matrix on element E_l^{FS} through

$$\int_{E_l^{\mathrm{FS}}} (v_h^s)_i g_i \nu_j^{s\to f} (u_h^s)_j [\rho^0]^f\,\mathrm{d}\Sigma = (\tilde{v}_i^s|_{E_l})^T [J_l^{2D} \rho_l^0 D_{g_i} \mathcal{M}_s^{2D} \nu_j^{s\to f}|_{E_l}]\tilde{u}_j^s|_{E_l}, \tag{42}$$

where ρ_l^0 and $\nu_j^{s\to f}|_{E_l}$ denote the density and normal vector on the boundary element E_l^{FS}, respectively, upon extracting $\tilde{v}_i^s|_{E_l}$ and $\tilde{u}_i^s|_{E_l}$.

We then evaluate the local matrices for A_f, A_p, M_s and M_f in Table 3 and obtain

$$\int_{K_k^{\mathrm{F}}} \rho^0 N^2 \frac{g_i (v_h^f)_i g_j (u_h^f)_j}{\|g\|^2}\,\mathrm{d}x = (\tilde{v}_i^f|_{K_k})^T [J_k D_{g_i/\|g\|} \rho_k^0 N_k^2 \mathcal{M}_f D_{g_j/\|g\|}]\tilde{u}_j^f|_{K_k}, \tag{43}$$

$$\int_{K_k^{\mathrm{F}}} -v_h^p p_h \kappa^{-1}\,\mathrm{d}x = (\tilde{v}^p|_{K_k})^T [-J_k \kappa_k^{-1} \mathcal{M}_p]\tilde{p}|_{K_k}, \tag{44}$$

$$\int_{K_k^{\mathrm{S}}} (v_h^s)_i (u_h^s)_i \rho^0\,\mathrm{d}x = (\tilde{v}_i^s|_{K_k})^T [J_k \rho_k^0 \mathcal{M}_s]\tilde{u}_i^s|_{K_k}, \tag{45}$$

$$\int_{K_k^{\mathrm{F}}} (v_h^f)_i (u_h^f)_i \rho^0\,\mathrm{d}x = (\tilde{v}_i^f|_{K_k})^T [J_k \rho_k^0 \mathcal{M}_f]\tilde{u}_i^f|_{K_k}, \tag{46}$$

where $D_{g_j/\|g\|}$ denotes a diagonal matrix whose diagonal entries are $g_j/\|g\|$; N_k^2 denotes the square of the Brunt-Väisälä frequency on element K_k.

3.4.2 Local matrices: A_{dg} and A_{dg}^{T}

Here, we discuss the integration between different variables. For the inner products between u_h^f and p_h for A_{dg} and $A_{\mathrm{dg}}^{\mathsf{T}}$ in Table 3, we evaluate the mass matrices $\mathcal{M}_{pf}$ and $\mathcal{M}_{fp}$,

$$\mathcal{M}_{pf} = (\mathcal{V}_p^{-1}(I_f))^T \mathcal{V}_f^{-1}(I_p), \quad \mathcal{M}_{fp} = (\mathcal{V}_f^{-1}(I_p))^T \mathcal{V}_p^{-1}(I_f),$$

where we refine the notation to indicate submatrices of $\mathcal{V}$; $\mathcal{V}(I)$ denotes the submatrix of $\mathcal{V}$ formed by columns indexed by $I \subseteq \{1, \ldots, N_p\}$. The selection of submatrix is based on the polynomial construction (Hesthaven & Warburton 2007, (10.6)). For instance, if the polynomial orders used for both u_h^f and p_h are the same, i.e., $p^f = p^p$, $I_f = I_p = \{1, \ldots, N_{pf}\}$; if $p^p = 1$ and $p^f = 2$, we have $N_{p^p} = 4$, $N_{pf} = 10$ and $I_f = \{1, 2, 3, 4\}$, $I_p = \{1, 2, 4, 7\}$. It is apparent that $\mathcal{M}_{pf} = \mathcal{M}_{fp}^T$.

Evaluating A_{dg} in Table 3 requires the evaluation of the local matrices on element K_k through

$$\int_{K_k^{\mathrm{F}}} (v_h^f)_j (\partial_{x_j} p_h) \,\mathrm{d}x = (\tilde{v}_j^f|_{K_k})^T [J_k \mathcal{M}_{fp} \mathsf{D}_j^p] \tilde{p}|_{K_k}, \tag{47}$$

$$\int_{K_k^{\mathrm{F}}} (v_h^f)_j g_j p_h \rho^0 \kappa^{-1} \,\mathrm{d}x = (\tilde{v}_j^f|_{K_k})^T [J_k D_{g_j} \rho_k^0 \kappa_k^{-1} \mathcal{M}_{fp}] \tilde{p}|_{K_k}, \tag{48}$$

where κ_k^{-1} denotes the inverse of the bulk modulus on element K_k. To evaluate $A_{\mathrm{dg}}^{\mathsf{T}}$ in Table 3, we also need to evaluate the local matrices on element K_k through

$$\int_{K_k^{\mathrm{F}}} (\partial_{x_j} v_h^p)(u_h^f)_j \,\mathrm{d}x = (\tilde{v}^p|_{K_k})^T [J_k (\mathsf{D}_j^p)^T \mathcal{M}_{pf}] \tilde{u}_j^f|_{K_k}, \tag{49}$$

$$\int_{K_k^{\mathrm{F}}} v_h^p g_j (u_h^f)_j \rho^0 \kappa^{-1} \,\mathrm{d}x = (\tilde{v}^p|_{K_k})^T [J_k \rho_k^0 \kappa_k^{-1} \mathcal{M}_{pf} D_{g_j}] \tilde{u}_j^f|_{K_k}. \tag{50}$$

3.4.3 Local matrices: E_{FS} and E_{FS}^{T}

For E_{FS} and $E_{\mathrm{FS}}^{\mathsf{T}}$, similar to Section 3.4.2, we introduce two new indices to construct $\mathcal{M}_{ps}^{2D}$ and $\mathcal{M}_{sp}^{2D}$ on the boundary elements associated with the fluid-solid boundary. The selection of the submatrix is based on (Hesthaven & Warburton 2007, Chapter 6). $\mathcal{M}_{ps}^{2D} = \mathcal{M}_{sp}^{2D\,\mathsf{T}}$ holds true as well. To evaluate $E_{\mathrm{FS}}^{\mathsf{T}}$ in Table 3, we need to compute the local matrix on boundary element E_l^{FS} through

$$\int_{E_l^{\mathrm{FS}}} (v_h^s)_j \nu_j^{s\to f} p_h \,\mathrm{d}\Sigma = (\tilde{v}_j^s|_{E_l})^{\mathsf{T}} [J_l^{2D} \nu_j^{s\to f} \mathcal{M}_{sp}^{2D}] \tilde{p}|_{E_l}, \tag{51}$$

upon extracting $\tilde{p}|_{E_l}$ on boundary element E_l^{FS}. To evaluate E_{FS} in Table 3, we need to evaluate the local matrix on boundary element E_l^{FS} through

$$\int_{E_l^{\mathrm{FS}}} v_h^p \nu_j^{f\to s} (u_h^s)_j \,\mathrm{d}\Sigma = (\tilde{v}^p|_{E_l})^{\mathsf{T}} [J_l^{2D} \nu_j^{f\to s} \mathcal{M}_{ps}^{2D}] \tilde{u}_j^s|_{E_l}, \tag{52}$$

upon extracting $\tilde{v}^p|_{E_l}$ on E_l^{FS}.

We now are able to build all the local matrices for the evaluation of the integrals in Table 3. We then assemble the global matrices from all these local matrices using similar standard techniques in Bathe (2006); Hughes (2012).

4 SELF-GRAVITATION AS AN N-BODY PROBLEM

We may treat the problem for solving self-gravitation as an N-body problem. We discretize the entire planet with many elements and consider them as individual bodies. The gravitational potential and field are then computed through the interaction between these bodies. We note that FMM is an ideal candidate for solving

an N-body problem. FMM reduces the complexity of the N-body problem from $O(N^2)$ to $O(N \log N)$ or even $O(N)$ (Greengard & Rokhlin 1987). We apply the FMM (Greengard & Rokhlin 1997; Gimbutas & Greengard 2011) to calculate the reference gravitional potential. In Section 6.1, we illustrate the high computational accuracy of such an approach. We employ `ExaFMM` (Yokota 2013), a massively parallel N-body problem solver, to solve for the incremental gravitational potential.

4.1 Reference gravitational potential

For calculating the reference gravitational potential and field, we need to evaluate two integrals (Dahlen & Tromp 1998, (3.2) and (3.3)). The N-body problem of gravitation requires the evaluation of

$$\Phi^0(\mathbf{x}_i) = -G \sum_{k=1}^{N_K} \frac{1}{\|\mathbf{x}_i - \mathbf{r}_k\|} \int_{K_k} \rho_k^0 \, \mathrm{d}x \tag{53}$$

for the potential and

$$g(\mathbf{x}_i) = -G \sum_{k=1}^{N_K} \frac{\mathbf{x}_i - \mathbf{r}_k}{\|\mathbf{x}_i - \mathbf{r}_k\|^{3/2}} \int_{K_k} \rho_k^0 \, \mathrm{d}x \tag{54}$$

for the field. Here, $\mathbf{x}_i$ denotes the location of the target vertex and $\mathbf{r}_k$ denotes the barycenter of element K_k.

4.2 Incremental gravitational potential

For calculating the incremental gravitational potential, we need to evaluate (23) containing both volume and boundary integral terms. Given the finite-element partitioning, $\mathcal{T}_h$, we approximate $S(u_h)$ in (2) via

$$S_{k_2}(u_h) = G \int_{K_{k_2}} \frac{\nabla \cdot (\rho_{k_2}^0(x) u_h(x))}{\|\mathbf{r}_{k_2} - x\|} \, \mathrm{d}x + \sum_{\substack{k_1=1 \\ k_1 \neq k_2}}^{N_K} \frac{G}{\|\mathbf{r}_{k_2} - \mathbf{r}_{k_1}\|} \int_{K_{k_1}} \nabla \cdot (\rho_{k_1}^0 u_h) \, \mathrm{d}x + \sum_{l_1=1}^{N_E} \frac{G}{\|\mathbf{r}_{k_2} - \mathbf{r}_{l_1}\|} \int_{E_{l_1}} \nu \cdot u_h \, [\rho_{l_1}^0]_-^+\big|_{E_{l_1}} \, \mathrm{d}\Sigma \tag{55}$$

and

$$S_{l_2}(u_h) = G \int_{E_{l_2}} \frac{\nu(x) \cdot u_h(x) \, [\rho_{l_2}^0(x)]_-^+\big|_{E_{l_2}}}{\|\mathbf{r}_{l_2} - x\|} \, \mathrm{d}\Sigma + \sum_{\substack{l_1=1 \\ l_1 \neq l_2}}^{N_E} \frac{G}{\|\mathbf{r}_{l_2} - \mathbf{r}_{l_1}\|} \int_{E_{l_1}} \nu \cdot u_h \, [\rho_{l_1}^0]_-^+\big|_{E_{l_1}} \, \mathrm{d}\Sigma + \sum_{k_1=1}^{N_K} \frac{G}{\|\mathbf{r}_{l_2} - \mathbf{r}_{k_1}\|} \int_{K_{k_1}} \nabla \cdot (\rho_{k_1}^0 u_h) \, \mathrm{d}x, \tag{56}$$

where k_1 and k_2 label the elements K_{k_1} and K_{k_2}, $S_{k_2}(u_h)$ is the incremental gravitational potential $S(u_h)$ at the barycenter of K_{k_2}, l_1 and l_2 label the triangular elements E_{l_1} and E_{l_2}, $\mathbf{r}_{l_1}$ and $\mathbf{r}_{l_2}$ denote the barycenters of E_{l_1} and E_{l_2}, and $[\rho_{l_1}^0]_-^+\big|_{E_{l_1}}$ denotes the initial density jump across E_{l_1}. The first terms in (55) and (56) indicate the self contribution.

Since the variation of $\nabla \cdot (\rho_{k_2}^0(x) u_h(x))$ is small on element K_{k_2}, we simplify the first term in (55) according to

$$G \int_{K_{k_2}} \frac{\nabla \cdot (\rho_{k_2}^0(x) u_h(x))}{\|\mathbf{r}_{k_2} - x\|} \, \mathrm{d}x \simeq G \frac{\int_{K_{k_2}} \nabla \cdot (\rho_{k_2}^0 u_h) \, \mathrm{d}x}{|K_{k_2}|} \int_{K_{k_2}} \frac{1}{\|\mathbf{r}_{k_2} - x\|} \, \mathrm{d}x,$$

where $|K_{k_2}|$ denotes the volume of element K_{k_2}. We let

$$\frac{1}{R_{k_2}} = \frac{1}{|K_{k_2}|} \int_{K_{k_2}} \frac{1}{\|\mathbf{r}_{k_2} - x\|} \, \mathrm{d}x,$$

operations	physical interpretations	corresponding formulae
$C_s\tilde{u}^s$	N bodies in $\overline{\Omega^{\mathrm{S}}}$	$\int_{\Omega^{\mathrm{S}}} \nabla\cdot(\rho^0 u_h^s)\,\mathrm{d}x,$ $\int_{\Sigma^{\mathrm{FS}}} \nu^{f\to s}\cdot u_h^s\,[\rho^0]^s\,\mathrm{d}\Sigma,$ $\int_{\Sigma^{\mathrm{SS}\cup\partial\tilde{X}^{\mathrm{S}}}} \nu\cdot u_h^s\,[\rho^0]_-^+\,\mathrm{d}\Sigma$
$C_f\tilde{u}^f$	N bodies in $\overline{\Omega^{\mathrm{F}}}$	$\int_{\Omega^{\mathrm{F}}} \nabla\cdot(\rho^0 u_h^f)\,\mathrm{d}x,$ $\int_{\Sigma^{\mathrm{FS}}} \nu^{s\to f}\cdot u^f\,[\rho^0]^f\,\mathrm{d}\Sigma,$ $\int_{\Sigma^{\mathrm{FF}\cup\partial\tilde{X}^{\mathrm{F}}}} \nu\cdot u_h^f\,[\rho^0]_-^+\,\mathrm{d}\Sigma$
S	solution for Poisson's equation	(23)
$(\tilde{v}^s)^{\mathsf{T}}C_s^{\mathsf{T}}(SC\tilde{u})$	incremental gravitational field in $\overline{\Omega^{\mathrm{S}}}$	$\int_{\Omega^{\mathrm{S}}} \nabla\cdot(\rho^0 v_h^s)S_k(u_h)\,\mathrm{d}x$ $+\int_{\Sigma^{\mathrm{FS}}} \nu^{f\to s}\cdot v_h^s S_l(u_h)[\rho^0]^s\,\mathrm{d}\Sigma$ $+\int_{\Sigma^{\mathrm{SS}\cup\partial\tilde{X}^{\mathrm{S}}}} \nu\cdot v_h^s S_l(u_h)[\rho^0]_-^+\,\mathrm{d}\Sigma$
$(\tilde{v}^s)^{\mathsf{T}}C_f^{\mathsf{T}}(SC\tilde{u})$	incremental gravational field in $\overline{\Omega^{\mathrm{F}}}$	$\int_{\Omega^{\mathrm{F}}} \nabla\cdot(\rho^0 v_h^f)S_k(u_h)\,\mathrm{d}x$ $+\int_{\Sigma^{\mathrm{FS}}} \nu^{s\to f}\cdot v_h^f S_l(u_h)[\rho^0]^f\,\mathrm{d}\Sigma$ $+\int_{\Sigma^{\mathrm{FF}\cup\partial\tilde{X}^{\mathrm{F}}}} \nu\cdot v_h^f S_l(u_h)[\rho^0]_-^+\,\mathrm{d}\Sigma$

Table 4. Implicit definition of the matrices. In the above, $\int_{\Omega^{\mathrm{S}}}=\sum_{k=1}^{N_K^{\mathrm{S}}}\int_{K_k^{\mathrm{S}}}$, $\int_{\Omega^{\mathrm{F}}}=\sum_{k=1}^{N_K^{\mathrm{F}}}\int_{K_k^{\mathrm{F}}}$, $\int_{\Sigma^{\mathrm{FS}}}=\sum_{l=1}^{N_E^{\mathrm{FS}}}\int_{E_l^{\mathrm{FS}}}$, $\int_{\Sigma^{\mathrm{SS}\cup\partial\tilde{X}^{\mathrm{S}}}}=\sum_{l=1}^{N_E^{\mathrm{S}}}\int_{E_l^{\mathrm{S}}}$, and $\int_{\Sigma^{\mathrm{FF}\cup\partial\tilde{X}^{\mathrm{F}}}}=\sum_{l=1}^{N_E^{\mathrm{F}}}\int_{E_l^{\mathrm{F}}}$.

and obtain

$$G\int_{K_{k_2}}\frac{\nabla\cdot(\rho^0_{k_2}(x)u_h(x))}{\|\mathbf{r}_{k_2}-x\|}\,\mathrm{d}x\simeq\frac{G}{R_{k_2}}\int_{K_{k_2}}\nabla\cdot(\rho^0_{k_2}u_h)\,\mathrm{d}x. \tag{57}$$

Similarly, we simplify the first term in (56) according to

$$G\int_{E_{l_2}}\frac{\nu(x)\cdot u_h(x)\;[\rho^0_{l_2}(x)]_-^+\big|_{E_{l_2}}}{\|\mathbf{r}_{l_2}-x\|}\,\mathrm{d}\Sigma\simeq\frac{G}{R_{l_2}}\int_{E_{l_2}}\nu\cdot u_h\;[\rho^0_{l_1}]_-^+\big|_{E_{l_1}}\,\mathrm{d}\Sigma, \tag{58}$$

with

$$\frac{1}{R_{l_2}}=\frac{1}{|E_{l_2}|}\int_{E_{l_2}}\frac{1}{\|\mathbf{r}_{l_2}-x\|}\,\mathrm{d}\Sigma,$$

where $|E_{l_2}|$ denotes the area of the boundary element E_{l_2}. Note that R_{k_2} in (57) and R_{l_2} in (58) can be precomputed on each element and surface. The second and third terms in (55) and (56) may be evaluated via FMM.

4.2.1 Solid planets

For the solid planets, we substitute (57) and (58) into (55) and (56), respectively. To evaluate (22) for a solid planet, we need to compute

$$\int_{\Omega^{\mathrm{S}}} v_h^s\cdot\nabla S(u_h^s)\rho^0\,\mathrm{d}x=-\sum_{k_2=1}^{N_K}\int_{K_{k_2}^{\mathrm{S}}}\left(\nabla\cdot(\rho^0_{k_2}v_h^s)\right)S_{k_2}(u_h^s)\,\mathrm{d}x$$
$$-\sum_{l_2=1}^{N_E}\int_{E_{l_2}^{\mathrm{S}}}\nu\cdot v_h^s S_{l_2}(u_h^s)\;[\rho^0_{l_2}]_-^+\big|_{E_{l_2}}\,\mathrm{d}\Sigma. \tag{59}$$

We add (59) into the matrix representation (37) and obtain

$$\left(A_{sg}-C_s^{\mathsf{T}}S_sC_s\right)\tilde{u}^s=\omega^2M_s\tilde{u}^s, \tag{60}$$

where $C_s\tilde{u}^s$ evaluates $S_{k_2}(u_h^s)$ and $S_{l_2}(u_h^s)$, S_s solves the N-body problem for the solid planet, and $C_s^{\mathsf{T}} S_s C_s \tilde{u}^s$ evaluates (59). The matrices C_s, C_s^{T}, S and their corresponding weak formulae are shown in Table 4. Here, of course, C_s and C_s^{T} do not include terms related the fluid-solid boundaries Σ^{FS}.

4.2.2 Planets with fluid regions

For a planet with fluid regions, we also substitute (57) and (58) into (55) and (56), respectively. To ensure the Hermitian property of the system, we carefully treat the fluid-solid boundary terms and evaluate the incremental gravitational potential $S(u_h)$ via (24) and obtain the volume integral contributions

$$\begin{aligned}
S_{k_2}(u_h) = {} & \frac{G}{R_{k_2}} \int_{K_{k_2}} \nabla \cdot (\rho_{k_2}^0 u_h)\, \mathrm{d}x + \sum_{l_1=1}^{N_E^{\mathrm{S}}} \frac{G}{\|\mathbf{r}_{k_2} - \mathbf{r}_{l_1}\|} \int_{E_{l_1}^{\mathrm{S}}} \nu \cdot u_h^s \, [\rho_{l_1}^0]_-^+\big|_{E_{l_1}} \, \mathrm{d}\Sigma \\
& + \sum_{\substack{k_1=1 \\ k_1 \neq k_2}}^{N_K^{\mathrm{S}}} \frac{G}{\|\mathbf{r}_{k_2} - \mathbf{r}_{k_1}\|} \int_{K_{k_1}^{\mathrm{S}}} \nabla \cdot (\rho_{k_1}^0 u_h^s)\, \mathrm{d}x + \sum_{l_1=1}^{N_E^{\mathrm{FS}}} \frac{G}{\|\mathbf{r}_{k_2} - \mathbf{r}_{l_1}\|} \int_{E_{l_1}^{\mathrm{FS}}} \nu^{f\to s} \cdot u_h^s \, [\rho_{l_1}^0]^s\big|_{E_{l_1}} \, \mathrm{d}\Sigma \\
& + \sum_{\substack{k_1=1 \\ k_2 \neq k_2}}^{N_K^{\mathrm{F}}} \frac{G}{\|\mathbf{r}_{k_2} - \mathbf{r}_{k_1}\|} \int_{K_{k_1}^{\mathrm{F}}} \nabla \cdot (\rho_{k_1}^0 u_h^f)\, \mathrm{d}x + \sum_{l_1=1}^{N_E^{\mathrm{FS}}} \frac{G}{\|\mathbf{r}_{k_2} - \mathbf{r}_{l_1}\|} \int_{E_{l_1}^{\mathrm{FS}}} \nu^{s\to f} \cdot u_h^f \, [\rho_{l_1}^0]^f\Big|_{E_{l_1}} \, \mathrm{d}\Sigma \\
& + \sum_{l_1=1}^{N_E^{\mathrm{F}}} \frac{G}{\|\mathbf{r}_{k_2} - \mathbf{r}_{l_1}\|} \int_{E_{l_1}^{\mathrm{F}}} \nu \cdot u_h^f \, [\rho_{l_1}^0]_-^+\big|_{E_{l_1}} \, \mathrm{d}\Sigma, \quad (61)
\end{aligned}$$

and boundary integral contributions

$$\begin{aligned}
S_{l_2}(u_h) = {} & \frac{G}{R_{l_2}} \int_{E_{l_2}} \nu \cdot u_h \, [\rho_{l_2}^0]_-^+\big|_{E_{l_2}} \, \mathrm{d}\Sigma + \sum_{\substack{l_1=1 \\ l_1 \neq l_2}}^{N_E^{\mathrm{S}}} \frac{G}{\|\mathbf{r}_{l_2} - \mathbf{r}_{l_1}\|} \int_{E_{l_1}^{\mathrm{S}}} \nu \cdot u_h^s \, [\rho_{l_1}^0]_-^+\big|_{E_{l_1}} \, \mathrm{d}\Sigma \\
& + \sum_{k_1=1}^{N_K^{\mathrm{S}}} \frac{G}{\|\mathbf{r}_{l_2} - \mathbf{r}_{k_1}\|} \int_{K_{k_1}^{\mathrm{S}}} \nabla \cdot (\rho_{k_1}^0 u_h^s)\, \mathrm{d}x + \sum_{l_1=1}^{N_E^{\mathrm{FS}}} \frac{G}{\|\mathbf{r}_{l_2} - \mathbf{r}_{l_1}\|} \int_{E_{l_1}^{\mathrm{FS}}} \nu^{f\to s} \cdot u_h^s \, [\rho_{l_1}^0]^s\big|_{E_{l_1}} \, \mathrm{d}\Sigma \\
& + \sum_{k_1=1}^{N_K^{\mathrm{F}}} \frac{G}{\|\mathbf{r}_{l_2} - \mathbf{r}_{k_1}\|} \int_{K_{k_1}^{\mathrm{F}}} \nabla \cdot (\rho_{k_1}^0 u_h^f)\, \mathrm{d}x + \sum_{l_1=1}^{N_E^{\mathrm{FS}}} \frac{G}{\|\mathbf{r}_{l_2} - \mathbf{r}_{l_1}\|} \int_{E_{l_1}^{\mathrm{FS}}} \nu^{s\to f} \cdot u_h^f \, [\rho_{l_1}^0]^f\Big|_{E_{l_1}} \, \mathrm{d}\Sigma \\
& + \sum_{\substack{l_1=1 \\ l_1 \neq l_2}}^{N_E^{\mathrm{F}}} \frac{G}{\|\mathbf{r}_{l_2} - \mathbf{r}_{l_1}\|} \int_{E_{l_1}^{\mathrm{F}}} \nu \cdot u_h^s \, [\rho_{l_1}^0]_-^+\big|_{E_{l_1}} \, \mathrm{d}\Sigma. \quad (62)
\end{aligned}$$

With (61) and (62), we have the full solution for the incremental gravitational potential. To evaluate (22) for a planet with fluid regions, we need to compute

$$\begin{aligned}
\int_{\tilde{X}} v_h \cdot \nabla S(u_h) \rho^0 \, \mathrm{d}x = {} & \int_{\Omega^{\mathrm{S}}} v_h^s \cdot \nabla S(u_h) \rho^0 \, \mathrm{d}x + \int_{\Omega^{\mathrm{F}}} v_h^f \cdot \nabla S(u_h) \rho^0 \, \mathrm{d}x = \\
& - \sum_{k_2=1}^{N_K^{\mathrm{S}}} \int_{K_{k_2}^{\mathrm{S}}} \left(\nabla \cdot (\rho_{k_2}^0 v_h^s)\right) S_{k_2}(u_h) \, \mathrm{d}x - \sum_{k_2=1}^{N_K^{\mathrm{F}}} \int_{K_{k_2}^{\mathrm{F}}} \Big(\nabla \cdot (\rho_{k_2}^0 v_h^f)\Big) S_{k_2}(u_h) \, \mathrm{d}x \\
& - \sum_{l_2=1}^{N_E^{\mathrm{S}}} \int_{E_{l_2}^{\mathrm{S}}} \nu \cdot v_h^s S_{l_2}(u_h) \, [\rho_{l_2}^0]_-^+\big|_{E_{l_2}} \, \mathrm{d}\Sigma - \sum_{l_2=1}^{N_E^{\mathrm{F}}} \int_{E_{l_2}^{\mathrm{F}}} \nu \cdot v_h^f S_{l_2}(u_h) \, [\rho_{l_2}^0]_-^+\big|_{E_{l_2}} \, \mathrm{d}\Sigma \\
& - \sum_{l_2=1}^{N_E^{\mathrm{FS}}} \int_{E_{l_2}^{\mathrm{FS}}} \nu^{f\to s} \cdot v_h^s S_{l_2}(u_h) \, [\rho_{l_2}^0]^s\big|_{E_{l_2}} \, \mathrm{d}\Sigma - \sum_{l_2=1}^{N_E^{\mathrm{FS}}} \int_{E_{l_2}^{\mathrm{FS}}} \nu^{s\to f} \cdot v_h^f S_{l_2}(u_h) \, [\rho_{l_2}^0]^f\Big|_{E_{l_2}} \, \mathrm{d}\Sigma. \quad (63)
\end{aligned}$$

We add (63) into the matrix representation (36) and obtain

$$\big(A_G - E_G A_p^{-1} E_G^{\mathsf{T}} - C^{\mathsf{T}} S C\big)\tilde{u} = \omega^2 M \tilde{u}, \tag{64}$$

with

$$C = \begin{pmatrix} C_s & C_f \end{pmatrix} \tag{65}$$

where $C\tilde{u} = C_s\tilde{u}^s + C_f\tilde{u}^f$ evaluates (61) and (62) to get $S_{k_2}(u_h)$ and $S_{l_2}(u_h)$, S solves the N-body problem, and $C^{\mathsf{T}}SC\tilde{u}$ evaluates (63). The matrices $C_s, C_s^{\mathsf{T}}, C_f, C_f^{\mathsf{T}}, S$ and their corresponding weak formulae are shown in Table 4.

4.3 Construction of the local matrices

Similar to Section 3.4, we list the local matrices in C_s,

$$\int_{K_k^{\mathrm{S}}} \partial_{x_i}(\rho^0(u_h^s)_i)\,\mathrm{d}x = (\mathbf{1}|_{K_k})^{\mathsf{T}}[J_k \mathcal{M}_s \mathsf{D}_i^s \rho_k^0]\tilde{u}_i^s|_{K_k}, \tag{66}$$

$$\int_{E_l^{\mathrm{FS}}} \nu_i^{f\to s}(u_h^s)_i \left[\rho^0\right]^s \,\mathrm{d}\Sigma = (\mathbf{1}|_{E_l})^{\mathsf{T}}[J_l^{2D}\nu_i^{f\to s}[\rho^0]_l^s \mathcal{M}_s^{2D}]\tilde{u}_i^s|_{E_l}, \tag{67}$$

$$\int_{E_l^{\mathrm{S}}} \nu_i(u_h^s)_i \left[\rho^0\right]_-^+ \,\mathrm{d}\Sigma = (\mathbf{1}|_{E_l})^{\mathsf{T}}[J_l^{2D}\nu_i([\rho^0]_-^+)_l \mathcal{M}_s^{2D}]\tilde{u}_i^s|_{E_l}, \tag{68}$$

and the local matrices in C_s^{T},

$$\int_{K_k^{\mathrm{S}}} [\partial_{x_i}(\rho^0(v_h^s)_i)] S_k(u_h)\,\mathrm{d}x = (\tilde{v}_i^s|_{K_k})^{\mathsf{T}}[J_k \rho_k^0 (\mathsf{D}_i^s)^{\mathsf{T}} \mathcal{M}_s S_k(\tilde{u})]\mathbf{1}|_{K_k}, \tag{69}$$

$$\int_{E_l^{\mathrm{FS}}} \nu_i^{f\to s}(v_h^s)_i S_l(u_h) \left[\rho^0\right]^s \,\mathrm{d}\Sigma = (\tilde{v}_i^s|_{E_l})^{\mathsf{T}}[J_l^{2D}\nu_i^{f\to s}\mathcal{M}_s^{2D}[\rho^0]_l^s S_l(\tilde{u})]\mathbf{1}|_{E_l}, \tag{70}$$

$$\int_{E_l^{\mathrm{S}}} \nu_i(v_h^s)_i S_l(u_h) \left[\rho^0\right]_-^+ \,\mathrm{d}\Sigma = (\tilde{v}_i^s|_{E_l})^{\mathsf{T}}[J_l^{2D}\nu_i \mathcal{M}_s^{2D}([\rho^0]_-^+)_l S_l(\tilde{u})]\mathbf{1}|_{E_l}, \tag{71}$$

where $\mathbf{1}$ denotes a vector of all ones. The construction of the local matrices in C_f and C_f^{T} is the same.

We now are able to build all the local matrices for the evaluation of the integrals in Table 4.

5 DETERMINING THE SEISMIC POINT SPECTRUM AND NORMAL MODES

Without loss of generality, we write (36) and its pure solid planet version (37) or (60) and (64) in the form of generalized eigenvalue problems:

$$A\tilde{u} = \lambda M \tilde{u}, \tag{72}$$

where M contains the relevant inner produtcs, and λ stands for ω^2. Since the explicit formation of A with self-gravitation requires excessive storage, it is mandatory to solve (72) via a matrix-free scheme, where A, M and M^{-1} are only accessed through matrix-vector multiplications. We combine several efficient parallel approaches to solve (72) with a matrix-free scheme.

Standard approaches for computing interior eigenpairs usually resort to exploiting spectral transformations, that is, shift-and-invert strategies (Parlett 1998). These require solving a linear system with $A - \sigma M$ when applying the filtered matrix, where σ denotes the pole. In practice, however, solving such linear systems often leads to a computational bottleneck on modern supercomputers with distributed memory. When computing interior eigenpairs, the shifted matrix $A - \sigma M$ is indefinite, and this significantly limits the applicability of iterative methods. Finding efficient parallel preconditioners can be a highly challenging task. For this reason, sparse direct methods are usually employed in this context to provide robust linear solvers. However, using direct solvers lowers the overall performance of the outer eigensolver substantially. We exemplify this issue in Shi et al. (2018).

Polynomial filtering techniques (Saad 2006; Fang & Saad 2012; Li et al. 2016) can be appealing as these

# of elements	116,085	1,136,447	2,019,017	3,081,551	4,035,022
MSE of Φ^0	2.133e-6	7.452e-8	1.784e-8	1.545e-8	1.430e-8
MSE of g	1.102e-3	1.848e-4	1.156e-4	8.781e-5	7.363e-5

Table 5. Errors in the gravitational calculation of a constant density ball.

do not involve solving linear systems with the indefinite matrices. Here, the bulk of the computations is carried out in the form of matrix-vector products. It has been shown that the polynomial filtering technique is ideally suited for solving large-scale 3D interior eigenvalue problems while it significantly enhances the memory and computational efficiency without loss of accuracy (Shi et al. 2018). In this paper, we adopt the polynomial filtering algorithms recently developed in Li et al. (2016, 2018); Shi et al. (2018) due to their simplicity and robustness. The details about our parallel algorithms and their performance can be found in Shi et al. (2018).

6 COMPUTATIONAL EXPERIMENTS

In this section, we first show the computational accuracy of our algorithm for the reference gravitational field using FMM. We then illustrate computational experiments yielding planetary normal modes with or without incremental gravitational potential using two supercomputers, Stampede2 (an Intel cluster) at the Texas Advanced Computing Center and Abel (a Cray XC30 cluster) at Petroleum Geo-Services. We show the convergence of our numerical formulation and approach for a constant elastic ball and PREM. The constant balls have a radius of 6,371 km, density $\rho^0 = 5.51 \times 10^3$ kg/m^3, P-wave speed $V_P = 10.0$ km/s and S-wave speed $V_S = 5.7735$ km/s. PREM used in our tests is modified in an isotropic model without attenuation, with $V_P = (V_{PV} + V_{PH})/2$ and $V_S = (V_{SV} + V_{SH})/2$. The ocean layer in PREM is replaced by crust. We compare our results with other one-dimensional solutions (Masters et al. 2011; Ye 2018). For the constant elastic balls, we compute normal modes with `MINEOS`. Since `MINEOS` has accuracy issues while dealing with fluid-solid boundaries, we utilize a radial FEM code to compute the normal modes (Ye 2018) of PREM as our reference. The discretization of the radial FEM code enables us to achieve high accuracy across the fluid-solid boundaries. While using radial FEM (Ye 2018), we use 2,550 elements with 11,900 degrees of freedom for the radial displacement. We also note that other normal modes computed from `MINEOS` may not be very accurate as shown in Section 6.3.2 since these normal modes need to be reorthogonalized with the modes related to the fluid-solid boundaries. The use of only 185 points by default in `MINEOS` may result in relatively larger errors in surface wave modes.

In our experiments, we show that the convergence tests are successful for all different normal modes in the frequency band considered up to 3.0 mHz. The modes computed in PREM are visualized in Appendix B. We then compute 3D normal modes directly in two different fully heterogeneous Earth models. Mode splitting and coupling are apparent and illustrated in Fig. 5.

6.1 Computational accuracy for the reference gravitational field

In this subsection, we illustrate the computational accuracy for the reference gravitational field using FMM. We begin with a simple constant-density ball. In Table 5, we show the FMM solution for a gravitational field of a constant density ball and a comparison with the closed-form solution. We note that FMM provides an accurate solution for this example.

We use PREM to build our Earth models on unstructured meshes with different sizes. In Table 6, we show the approximation errors of different three-layer models, which contain two major discontinuities (CMB and ICB) when comparing with the semi-analytical solution. In Fig. 4, we show the comparison of the gravitational field computed via FMM with the semi-analytical solution in PREM.

In Table 7, we show the approximation errors of different seven-layer models which contain six major discontinuities (Moho, top of Low Velocity Zone (LVZ), bottom of LVZ, 660, CMB and ICB) with the semi-analytical solution.

# of elements	5,800	57,490	503,882	1,136,447	2,093,055	5,549,390	7,825,918
MSE of Φ^0	3.604e-3	2.635e-4	4.071e-5	2.092e-5	1.354e-5	4.059e-6	2.396e-9
MSE of g	5.805e-2	5.479e-3	7.320e-4	3.218e-4	2.068e-4	9.524e-5	5.609e-5

Table 6. Errors of three-layer approximations in the gravitational calculation.

6.2 Computational accuracy for self-gravitation

Here, we show a convergence analysis for computing normal modes of a non-rotating and self-gravitating planet.

6.2.1 Solid models

We present our results for purely solid models with self-gravitation. In Tables 8 and 10, we list the number of elements '#elm.' as well as the problem sizes (labeled as 'size of A' for the solid cases and 'size of A_G' and 'size of A_p' for the Earth examples), the number of surfaces '#surf.', the size of S_s or S, a tight bound of the smallest and the largest eigenvalues $(\lambda_{\min}, \lambda_{\max})$, the degree of the polynomial filter 'deg', the number of the Lanczos iterations required '#it', and the number of the normal modes computed '#eigs'.

Since the pure solid models do not generate any essential spectra, we can directly compute the lowest-frequency normal modes. We note that the length $(\lambda_{\max} - \lambda_{\min})$ of the spectrum grows with the size of the problem determined by the discretization.

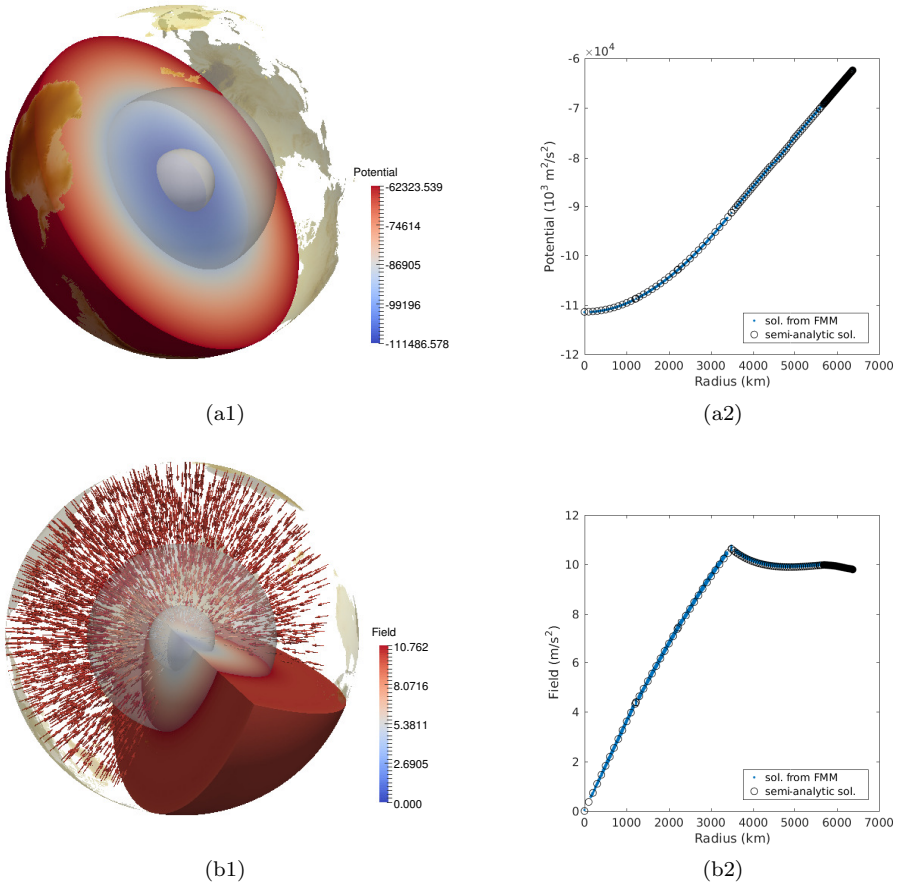

(a1) (a2)

(b1) (b2)

Figure 4. Comparison between the semi-analytical and FMM solutions: (a1) FMM gravitational potential; (a2) comparison in the radial direction; (b1) FMM gravitational field; (b2) comparison in the radial direction.

# of elements	2,031,729	5,018,249	8,043,617	12,479,828	16,560,615
MSE of Φ^0	2.333e-7	4.485e-8	1.286e-8	9.785e-9	5.548e-9
MSE of g	1.926e-4	8.606e-5	5.186e-5	4.036e-6	3.394e-5

Table 7. Errors of seven-layer approximations in the gravitational calculation.

In Table 9, we show convergence results for different solid models using P1 elements, that is, the finite-element polynomial orders $p^s = p^f = p^p = 1$ are used throughout this work. Comparing with 1D results, we observe that our computational results do converge. We accept relative errors of about 0.1%.

In Table 10, we list test cases for different solid models using P2 elements , that is, the finite-element polynomial orders $p^s = p^f = p^p = 2$ are used throughout this work. From experiments C1p2 to C5p2, we double the number of elements and obtain proper convergence results in Table 11. We show that even with about 330,000 elements, we are able to achieve four digits of accuracy.

6.2.2 PREM

Here, we include a liquid outer core using PREM and the presence of the essential spectrum. Because the degree of the polynomial order is quite high when using P2 elements, we perform our convergence test using P1 elements only.

In Table 12, we show test cases for PREM. We roughly double the number of elements from E1p1 to E7p1. In Table 13, we argue convergence by comparing with 1D results. For PREM with self-gravitation, we accept relative errors of around 0.1%.

6.3 Computational accuracy for the Cowling approximation

Here, we only include the reference gravitational field. Without including the computation of the perturbed gravitational potential, the computational costs are significantly reduced. We, again, show computational tests for different models.

6.3.1 Solid models

For tests for the solid models in Table 14, we here compute the interior normal modes with the reference gravitational field only.

In Table 15, we note that experiments C9p1 and C6p2 have similar numbers of degrees of freedom but the numerical accuracy of C6p2 is clearly higher. We have achieved five digits of accuracy in these tests using P2 elements.

We compare frequencies of different spheroidal modes from experiment C7p2 in Tables 17 and 19. Frequencies of different toroidal modes from experiment C7p2 are compared in Tables 18 and 20. Both tests show that we are able to achieve five digits of accuracy for all the modes in the range of $[2.0, 3.0]$mHz.

6.3.2 PREM

For the tests presented in Table 21, we compute the interior normal modes with the reference gravitational field as before.

Exp.	#elm.	size of A	#surf.	size of S_s	$(\lambda_{\min}, \lambda_{\max})$	(deg,#it)	#eigs
C1p1	5,123	2,727	392	5,515	(-1.02e-7,5.01e-3)	(14,192)	70
C2p1	21,093	10,644	956	22,049	(-5.66e-8,1.20e-2)	(25,232)	92
C3p1	39,273	19,131	956	40,229	(-5.74e-8,1.97e-2)	(34,252)	92
C4p1	105,115	51,933	3,608	108,723	(-2.51e-8,3.47e-2)	(50,252)	92
C5p1	495,099	242,721	14,888	509,987	(-7.58e-8,1.04e-1)	(108,272)	92

Table 8. Test cases for different solid models with self-gravitation using P1 elements for the frequency range $[0.1, 1.0]$mHz.

Exp.	${}_0T_2$	${}_0S_2$	${}_1S_1$	${}_0S_0$	${}_0T_3$	${}_0S_3$	${}_1S_2$	${}_0T_4$	${}_0S_4$
C1p1	0.3724	0.4178	0.4600	0.5105	0.5881	0.6322	0.6900	0.7973	0.8359
C2p1	0.3653	0.4112	0.4511	0.5053	0.5692	0.6052	0.6708	0.7587	0.7791
C3p1	0.3643	0.4103	0.4502	0.5053	0.5665	0.6017	0.6680	0.7527	0.7721
C4p1	0.3622	0.4089	0.4472	0.5035	0.5612	0.5932	0.6622	0.7424	0.7526
C5p1	0.3612	0.4086	0.4460	0.5035	0.5587	0.5899	0.6596	0.7374	0.7445
mineos1D	0.3607	0.4087	0.4456	0.5040	0.5574	0.5885	0.6582	0.7348	0.7406

Table 9. Convergence tests for different solid models in Table 8 with self-gravitation for P1 elements.

Exp.	#elm.	size of A	#surf.	size of S_s	$(\lambda_{\min}, \lambda_{\max})$	(deg,#it)	#eigs
C1p2	19,073	75,888	956	20,029	(-2.12e-7,1.60e-1)	(44,512)	92
C2p2	40,378	170,025	3,608	43,986	(-6.37e-9,2.36e-1)	(58,492)	92
C3p2	80,554	335,103	5,924	86,478	(-2.25e-8,3.73e-1)	(81,492)	92
C4p2	152,426	645,687	14,888	167,314	(-3.04e-9,7.14e-1)	(129,492)	92
C5p2	334,193	1,360,140	14,888	349,081	(-3.74e-8,1.30e0)	(200,492)	92

Table 10. Test cases for different solid models with self-gravitation using P2 elements for the frequency range $[0.1, 1.0]$mHz.

Exp.	${}_0T_2$	${}_0S_2$	${}_1S_1$	${}_0S_0$	${}_0T_3$	${}_0S_3$	${}_1S_2$	${}_0T_4$	${}_0S_4$
C1p2	0.3619	0.4100	0.4473	0.5094	0.5594	0.5908	0.6605	0.7376	0.7439
C2p2	0.3610	0.4090	0.4459	0.5042	0.5579	0.5889	0.6587	0.7355	0.7413
C3p2	0.3609	0.4089	0.4463	0.5042	0.5577	0.5888	0.6585	0.7352	0.7410
C4p2	0.3608	0.4088	0.4456	0.5041	0.5575	0.5886	0.6583	0.7349	0.7408
C5p2	0.3608	0.4087	0.4456	0.5041	0.5575	0.5885	0.6583	0.7349	0.7407
mineos1D	0.3607	0.4087	0.4456	0.5040	0.5574	0.5885	0.6582	0.7348	0.7406

Table 11. Convergence tests for the solid models in Table 10 with self-gravitation using P2 elements.

Exp.	#elm.	size of A_G	size of A_p	#surf.	size of S_s	$(\lambda_{\min}, \lambda_{\max})$	(deg,#it)	#eigs
E1p1	9,721	7,590	887	2,304	12,025	(-8.70e-5,5.04e-2)	(187,392)	64
E2p1	20,466	14,736	974	4,956	25,422	(-7.69e-5,5.20e-2)	(182,372)	72
E3p1	42,828	30,384	3,171	8,172	51,000	(-8.27e-5,1.74e-1)	(342,452)	83
E4p1	83,354	63,225	5,298	22,104	105,458	(-1.26e-4,5.81e-1)	(745,452)	88
E5p1	157,057	96,852	6,771	22,104	179,161	(-1.18e-4,6.15e-1)	(747,492)	88
E6p1	303,218	164,673	10,077	22,104	325,322	(-1.05e-4,5.75e-1)	(685,492)	88
E7p1	639,791	361,587	21,824	60,288	700,079	(-1.12e-4,6.18e-1)	(685,492)	88
E8p1	1,972,263	1,086,702	70,429	150,288	2,122,551	(-1.10e-4,2.87e0)	(1565,492)	88

Table 12. Test cases for different Earth models with self-gravitation using P1 elements for the frequency range $[0.1, 1.0]$mHz.

Exp.	${}_0S_2$	${}_0T_2$	${}_2S_1$	${}_0S_3$	${}_0T_3$
E1p1	0.3284	0.3953	0.4179	0.5242	0.6241
E2p1	0.3229	0.3921	0.4149	0.5077	0.6146
E3p1	0.3177	0.3884	0.4113	0.4932	0.6062
E4p1	0.3166	0.3842	0.4090	0.4903	0.5980
E5p1	0.3137	0.3845	0.4085	0.4863	0.5962
E6p1	0.3126	0.3840	0.4080	0.4768	0.5945
E7p1	0.3116	0.3834	0.4073	0.4742	0.5933
E8p1	0.3112	0.3829	0.4067	0.4721	0.5920
FEM1D	0.3110	0.3826	0.4063	0.4713	0.5912
mineos1D	0.3107	0.3823	0.4062	0.4709	0.5908

Table 13. Convergence tests for different Earth models in Table 12 with self-gravitation using P1 elements.

Exp.	#elm.	size of A	$(\lambda_{\min}, \lambda_{\max})$	range	(deg,#it)	#eigs
C9p1	16,036,734	7,954,392	(-9.63e-6,3.52e0)	$[1.5, 2.0]$	(991,1152)	323
C6p2	2,067,539	8,419,194	(-1.38e-5,4.55e0)	$[1.5, 2.0]$	(790,1692)	323
C7p2	4,133,442	16.771,833	(-1.78e-5,8.55e0)	$[1.5, 2.0]$	(1108,1692)	323
C7p2	4,133,442	16.771,833	(-1.78e-5,8.55e0)	$[2.0, 2.5]$	(1057,2572)	482
C7p2	4,133,442	16.771,833	(-1.78e-5,8.55e0)	$[2.5, 3.0]$	(1056,3792)	723

Table 14. Test cases for different solid models with the reference gravitational field. The first three and the last two tests compute normal modes in the range of $[1.5, 2.0]$mHz and $[2.0, 2.5]$mHz, $[2.5, 3.0]$mHz, respectively.

In Tables 22 and 23, we show results computed in a frequency range $[1.5, 2.0]$mHz. Experiments E9p1 and E6p2 have the same number of degrees of freedom, but E6p2 provides more accurate solutions for different modes using P2 elements. We note that in experiment E7p2 we have achieved five digits of accuracy.

In Tables 24 and 25, we provide eigenfrequencies associated with spheroidal and toroidal modes computed in the frequency range $[2.0, 2.5]$mHz. In Tables 26 and 27, we provide eigenfrequencies associated with spheroidal and toroidal modes computed in the frequency range $[2.5, 3.0]$mHz. In our experiments, the relative errors of such a calculation are around 10^{-4}.

6.4 Fully heterogeneous models

We construct two other, 3D Earth models using MIT's mantle tomographic results (Burdick et al. 2017) and crust 1.0 (Laske et al. 2013). The core model is based on PREM. The mantle seismic reference wave speeds are based on AK135 (Kennett et al. 1995). One model is obtained by combining MIT's mantle tomographic model and PREM for the core and density. The other one replaces PREM's crust by crust 1.0, which is shown in Fig. 2. In Table 28, we show the information of three different tests for these three different Earth models. Since with similar degrees of freedom, the largest eigenvalue of the MIT model with the 3D crust is much larger than the ones of the other two models, we expect that significant mode coupling and splitting occur (Deuss & Woodhouse 2001; Romanowicz et al. 2008; Beghein et al. 2008; Irving et al. 2009; Koelemeijer et al. 2012; Nader et al. 2015; Yang & Tromp 2015; Akbarashrafi et al. 2017; Al-Attar et al. 2018).

We visualize the eigenfunctions of different modes for observation. The normal modes computed in the two MIT models are non-degenerate. In Fig. 5, we compare different modes computed in the three models in the frequency range $[2.0, 2.5]$mHz. Since the background models have only slight differences, some of the eigenfrequencies are similar amongst PREM and the MIT models. We illustrate most of the modes computed in PREM in Appendix B. In Fig. 5(a), we observe that, even at low frequencies, weak mode splitting occurs for surface wave modes, including ${}_2S_8$, ${}_0S_{13}$, ${}_0T_{14}$ and ${}_1T_7$. We also report that no coupled modes are observed in $[2.0, 2.18]$mHz. In Figs. 5(b-d), we show the different modes in $[2.18, 2.28]$, $[2.28, 2.38]$ and $[2.38, 2.48]$mHz, respectively. The splitting of most surface wave modes becomes larger with increasing frequency. However, since modes like ${}_1S_{10}$ (strong at the core-mantle boundary) in Fig. 5(a), ${}_0c_4$ (an inner core toroidal mode) and ${}_3S_5$ (an ICB Stoneley mode) in Fig. 5(c), are not sensitive to the crust and upper mantle structure, no clear splitting is observed. We observe coupled modes in Figs. 5(b-d) computed in the MIT model with the 3D crust. The eigenfunction of one mode in Fig. 5(b) shows that ${}_0S_{14}$ and ${}_2T_2$ are coupled. The ${}_0T_{15}$ and ${}_8S_1$ near ${}_0S_{14}$ and ${}_2T_2$ are isolated multiplets. The eigenfunctions of the two modes in Fig. 5(c) show that ${}_1S_{11}$ and ${}_0T_{16}$ are coupled. The ${}_0S_{15}$ near ${}_1S_{11}$ and ${}_0T_{16}$ is an isolated multiplet. These coupled modes are interesting because ${}_1S_{11}$ illustrated in Fig. B.2 is clearly sensitive to the core-mantle

Exp.	${}_4S_1$	${}_0S_{10}$	${}_2S_4$	${}_1S_6$	${}_3S_3$	${}_0S_{11}$	${}_4S_2$	${}_2S_5$	${}_1S_7$	${}_0S_{12}$	${}_5S_1$
C9p1	1.5431	1.5830	1.5917	1.6252	1.7002	1.7190	1.7534	1.7829	1.8388	1.8551	1.8708
C6p2	1.5413	1.5784	1.5898	1.6240	1.6992	1.7131	1.7508	1.7803	1.8368	1.8476	1.8701
C7p2	1.5413	1.5783	1.5898	1.6240	1.6992	1.7131	1.7507	1.7803	1.8368	1.8476	1.8701
mineos1D	1.5412	1.5783	1.5898	1.6239	1.6991	1.7130	1.7507	1.7802	1.8367	1.8475	1.8700

Table 15. Comparison of different spheroidal modes for different solid models with the reference gravitational field in $[1.5, 2.0]$mHz.

Exp.	${}_2T_2$	${}_0T_9$	${}_1T_5$	${}_0T_{10}$	${}_2T_3$	${}_1T_6$	${}_3T_1$	${}_0T_{11}$	${}_2T_4$	${}_1T_7$
C9p1	1.5184	1.5469	1.5823	1.7035	1.7164	1.7576	1.7803	1.8592	1.9091	1.9314
C6p2	1.5166	1.5449	1.5795	1.7008	1.7138	1.7548	1.7774	1.8558	1.9055	1.9277
C7p2	1.5165	1.5448	1.5794	1.7008	1.7137	1.7548	1.7774	1.8557	1.9054	1.9276
mineos1D	1.5165	1.5448	1.5794	1.7008	1.7137	1.7547	1.7773	1.8556	1.9054	1.9276

Table 16. Comparison of different spheroidal modes for different solid models with the reference gravitational field in $[1.5, 2.0]$mHz.

boundary and the fundamental Love mode ${}_0T_{16}$ illustrated in Fig. B.6 can be measured at the surface. The left mode in Fig. 5(d) is a ${}_0S_{16}$ and ${}_1T_9$ coupled mode. The right mode in Fig. 5(d) is a ${}_6S_2$ and ${}_0T_{17}$ coupled mode. This mode is also very interesting because ${}_6S_2$ illustrated in Fig. B.4 is an inner core mode and the fundamental Love mode ${}_0T_{17}$ illustrated in Fig. B.6 can be detected at the surface. Since the relative wave speed variations of the MIT tomographic model vary roughly from -1.4% to 1.4% in the upper mantle and the crust's thickness is small, strong mode coupling occurs only to two modes. In this frequency range $[2.0, 2.5]$mHz, the width of each multiplet is small and no significant coupling between three and more modes is observed.

7 CONCLUSION

We developed and exploited a novel weak formulution as well as a massively parallel algorithm to compute the seismic point spectrum of the elastic-gravitational system describing the normal modes of terrestrial planets. The system is discretized with a Continuous Galerkin method, more precisely, with the mixed FEM on unstructured tetrahedral meshes on the fluid and solid regions. We included self-gravitation via a FMM. We used several computational experiments to demonstrate the achievable accuracy of our proposed approach. We performed convergence tests for constant elastic ball models and PREM. We carried out computational experiments in fully heterogeneous Earth models accounting for a 3D crust. There is no clear computational barrier for our algorithm to further increase the degrees of freedom (Shi et al. 2018) and, hence, we expect that modes at yet higher frequencies may be computed. Our algorithm allows different discretization methods such as the spectral element method (Komatitsch & Tromp 2002). Our algorithm enables the further study of seismic normal modes in models far from spherically symmetric structures.

ACKNOWLEDGEMENT

This research was supported by the Simons Foundation under the MATH+X program, the National Science Foundation under grant DMS-1559587, the members of the Geo-Mathematical Imaging Group at Rice University, and XSEDE research allocation TG-EAR170019. J.S. would like to thank Petroleum Geo-Services for using their supercomputer Abel and Hongjian Fang for providing the MIT model. The work by R.L. was performed under the auspices of the U.S. Department of Energy by Lawrence Livermore National Laboratory under Contract DE-AC52-07NA27344 (LLNL-JRNL-xxxxxx, the exact number will be updated). Y.X. and Y.S. were supported by NSF grants DMS-1521573, CCF-1505970 and CCF-1812695.

Exp.	${}_6S_1$	${}_1S_8$	${}_0S_{14}$	${}_2S_7$	${}_5S_2$	${}_4S_4$	${}_3S_5$	${}_1S_9$	${}_0S_{15}$	${}_6S_2$	${}_2S_9$
C7p2	2.0132	2.0384	2.1162	2.1709	2.1720	2.1867	2.1961	2.2299	2.2502	2.2691	2.3729
mineos1D	2.0131	2.0383	2.1161	2.1708	2.1719	2.1866	2.1960	2.2299	2.2501	2.2691	2.3728

Table 17. Different spheroidal modes from experiment C7p2 with the reference gravitational field in $[2.0, 2.5]$mHz.

Exp.	${}_0T_{12}$	${}_2T_5$	${}_1T_8$	${}_0T_{13}$	${}_3T_3$	${}_4T_1$	${}_1T_9$	${}_2T_6$	${}_0T_{14}$	${}_3T_4$	${}_1T_{10}$
C7p2	2.0098	2.0929	2.0984	2.1633	2.1888	2.2237	2.2674	2.2771	2.3161	2.3863	2.4350
mineos1D	2.0098	2.0929	2.0983	2.1632	2.1887	2.2237	2.2673	2.2770	2.3161	2.3862	2.4349

Table 18. Different toroidal modes from experiment C7p2 with the reference gravitational field in $[2.0, 2.5]$mHz.

Exp.	${}_0S_{17}$	${}_2S_9$	${}_6S_3$	${}_1S_{11}$	${}_5S_4$	${}_3S_7$	${}_0S_{18}$	${}_4S_6$	${}_7S_2$	${}_1S_8$	${}_1S_{12}$	${}_2S_{10}$
C7p2	2.5181	2.5783	2.5786	2.5906	2.6027	2.6077	2.6519	2.6725	2.6775	2.6862	2.7631	2.7851
mineos1D	2.5179	2.5782	2.5785	2.5905	2.6026	2.6076	2.6517	2.6725	2.6776	2.6861	2.7630	2.7850

Table 19. Different spheroidal modes from experiment C7p2 with the reference gravitational field in $[2.5, 3.0]$mHz.

Exp.	${}_3T_5$	${}_1T_{11}$	${}_0T_{16}$	${}_2T_8$	${}_4T_3$	${}_5T_1$	${}_1T_{11}$	${}_3T_6$	${}_0T_{16}$	${}_2T_9$	${}_4T_4$	${}_5T_2$
C7p2	2.5797	2.6013	2.6204	2.6376	2.6556	2.6956	2.7665	2.7699	2.7719	2.8148	2.8572	2.9095
mineos1D	2.5796	2.6012	2.6203	2.6375	2.6556	2.6955	2.7664	2.7698	2.7718	2.8146	2.8571	2.9093

Table 20. Different toroidal modes from experiment C7p2 with the reference gravitational field in $[2.5, 3.0]$mHz.

Exp.	#elm.	size of A_G	size of A_p	$(\lambda_{\min}, \lambda_{\max})$	range (mHz)	(deg,#it)	#eigs
E9p1	16,436,247	9,037,671	658,285	(-9.13e-7,3.10e+1)	$[1.5, 2.0]$	(2852,1232)	326
E6p2	1,972,263	8,400,630	522,705	(-4.52e-7,2.00e+1)	$[1.5, 2.0]$	(2250,1252)	345
E7p2	4,094,031	17,469,666	1,181,103	(-1.77e-6,5.37e+1)	$[1.5, 2.0]$	(2540,1172)	320
E7p2	4,094,031	17,469,666	1,181,103	(-1.77e-6,5.37e+1)	$[2.0, 2.5]$	(4054,1892)	528
E8p2	8,000,777	34,282,806	2,299,704	(-5.03e-6,1.26e+2)	$[2.5, 3.0]$	(5709,2712)	754

Table 21. Test cases for different Earth models with the reference gravitational field.

Exp.	${}_2S_5$	${}_1S_6$	${}_0S_9$	${}_1S_7$	${}_2S_6$	${}_0S_{10}$	${}_4S_2$	${}_6S_1$	${}_1S_8$	${}_0S_{11}$	${}_2S_7$
E9p1	1.5356	1.5437	1.5920	1.6774	1.7039	1.7408	1.7544	1.7642	1.8233	1.8775	1.8907
E6p2	1.5335	1.5402	1.5880	1.6719	1.7019	1.7359	1.7509	1.7556	1.8153	1.8727	1.8883
E7p2	1.5333	1.5398	1.5884	1.6715	1.7016	1.7365	1.7513	1.7552	1.8149	1.8726	1.8880
FEM1D	1.5335	1.5400	1.5884	1.6718	1.7018	1.7366	1.7513	1.7550	1.8152	1.8727	1.8882
mineos1D	1.5312	1.5398	1.5863	1.6715	1.6987	1.7339	1.7512	1.7550	1.8148	1.8696	1.8845

Table 22. Tests of spheroidal modes for different Earth models in Table 21 with the reference gravitational field in $[1.5, 2.0]$mHz.

Exp.	${}_1T_4$	${}_0T_{10}$	${}_0T_{11}$	${}_1T_5$	${}_0T_{12}$	${}_1T_6$	${}_0T_{13}$
E9p1	1.6013	1.6298	1.7550	1.7683	1.8775	1.9458	1.9981
E6p2	1.5983	1.6266	1.7509	1.7645	1.8718	1.9411	1.9923
E7p2	1.5975	1.6268	1.7513	1.7637	1.8732	1.9401	1.9931
FEM1D	1.5972	1.6269	1.7515	1.7633	1.8735	1.9397	1.9934
mineos1D	1.5968	1.6234	1.7473	1.7629	1.8686	1.9391	1.9877

Table 23. Tests of toroidal modes for different Earth models in Table 21 with the reference gravitational field in $[1.5, 2.0]$mHz.

Exp.	${}_0S_{12}$	${}_7S_1$	${}_2S_8$	${}_4S_3$	${}_5S_2$	${}_0S_{13}$	${}_1S_{10}$	${}_5S_3$	${}_0S_{14}$	${}_8S_1$	${}_2S_9$	${}_3S_5$
E7p2	2.0008	2.0189	2.0741	2.0765	2.1133	2.1237	2.1647	2.1892	2.2426	2.2524	2.2555	2.2855
FEM1D	2.0009	2.0186	2.0743	2.0760	2.1127	2.1239	2.1650	2.1886	2.2429	2.2518	2.2556	2.2846
mineos1D	1.9974	2.0183	2.0702	2.0759	2.1121	2.1200	2.1647	2.1878	2.2386	2.2513	2.2511	2.2846

Table 24. Computation of spheroidal modes for experiment E7p2 with the reference gravitational field in $[2.0, 2.5]$mHz.

Exp.	${}_0T_{14}$	${}_1T_7$	${}_2T_1$	${}_0T_{15}$	${}_2T_2$	${}_1T_8$	${}_2T_3$	${}_0T_{16}$	${}_2T_4$	${}_0T_{17}$	${}_1T_9$
E7p2	2.1112	2.1198	2.2072	2.2282	2.2496	2.2975	2.3148	2.3432	2.4001	2.4576	2.4711
FEM1D	2.1115	2.1192	2.2064	2.2278	2.2504	2.2970	2.3141	2.3437	2.3992	2.4582	2.4706
mineos1D	2.1050	2.1185	2.2059	2.2209	2.2490	2.2960	2.3134	2.3355	2.3985	2.4491	2.4694

Table 25. Computation of toroidal modes for experiment E7p2 with the reference gravitational field in $[2.0, 2.5]$mHz.

Exp.	${}_7S_2$	${}_3S_6$	${}_1S_{12}$	${}_0S_{17}$	${}_2S_{11}$	${}_4S_6$	${}_0S_{18}$	${}_3S_7$	${}_5S_5$	${}_2S_{12}$	${}_1S_{13}$	${}_0S_{19}$
E8p2	2.5550	2.5673	2.5725	2.5832	2.6033	2.6850	2.6905	2.7042	2.7272	2.7701	2.7850	2.7952
FEM1D	2.5554	2.5676	2.5731	2.5808	2.6026	2.6842	2.6879	2.7044	2.7181	2.7695	2.7855	2.7926
mineos1D	2.5551	2.5659	2.5727	2.5755	2.5972	2.6842	2.6822	2.7022	2.7277	2.7636	2.7851	2.7866

Table 26. Computation of spheroidal modes for experiment E8p2 with the reference gravitational field in $[2.5, 3.0]$mHz.

Exp.	${}_2T_5$	${}_0T_{18}$	${}_2T_6$	${}_1T_{10}$	${}_0T_{19}$	${}_2T_7$	${}_0T_{20}$	${}_1T_{11}$	${}_2T_8$	${}_1T_{12}$
E8p2	2.5041	2.5754	2.6296	2.6391	2.6888	2.7739	2.8016	2.8036	2.9348	2.9647
FEM1D	2.5050	2.5718	2.6304	2.6394	2.6848	2.7746	2.7971	2.8039	2.9355	2.9649
mineos1D	2.5041	2.5617	2.6295	2.6397	2.6738	2.7736	2.7851	2.8022	2.9344	2.9630

Table 27. Computation of toroidal modes for experiment E8p2 with the reference gravitational field in $[2.5, 3.0]$mHz.

Exp.	#elm.	size of A_G	size of A_p	$(\lambda_{\min}, \lambda_{\max})$	range (mHz)	(deg,#it)	#eigs
E7p2	4,094,031	17,469,666	1,181,103	(-1.77e-6,5.37e+1)	$[2.0, 2.5]$	(4054,1892)	528
MIT	4,048.932	16,578,945	879,067	(-2.55e-5,2.47e+1)	$[2.0, 2.5]$	(2674,1912)	520
MIT+3D crust	4,044,225	16,550,922	878,808	(-6.02e-5,1.45e+2)	$[2.0, 2.5]$	(6984,1912)	550

Table 28. Test cases for three different Earth models with the reference gravitational field.

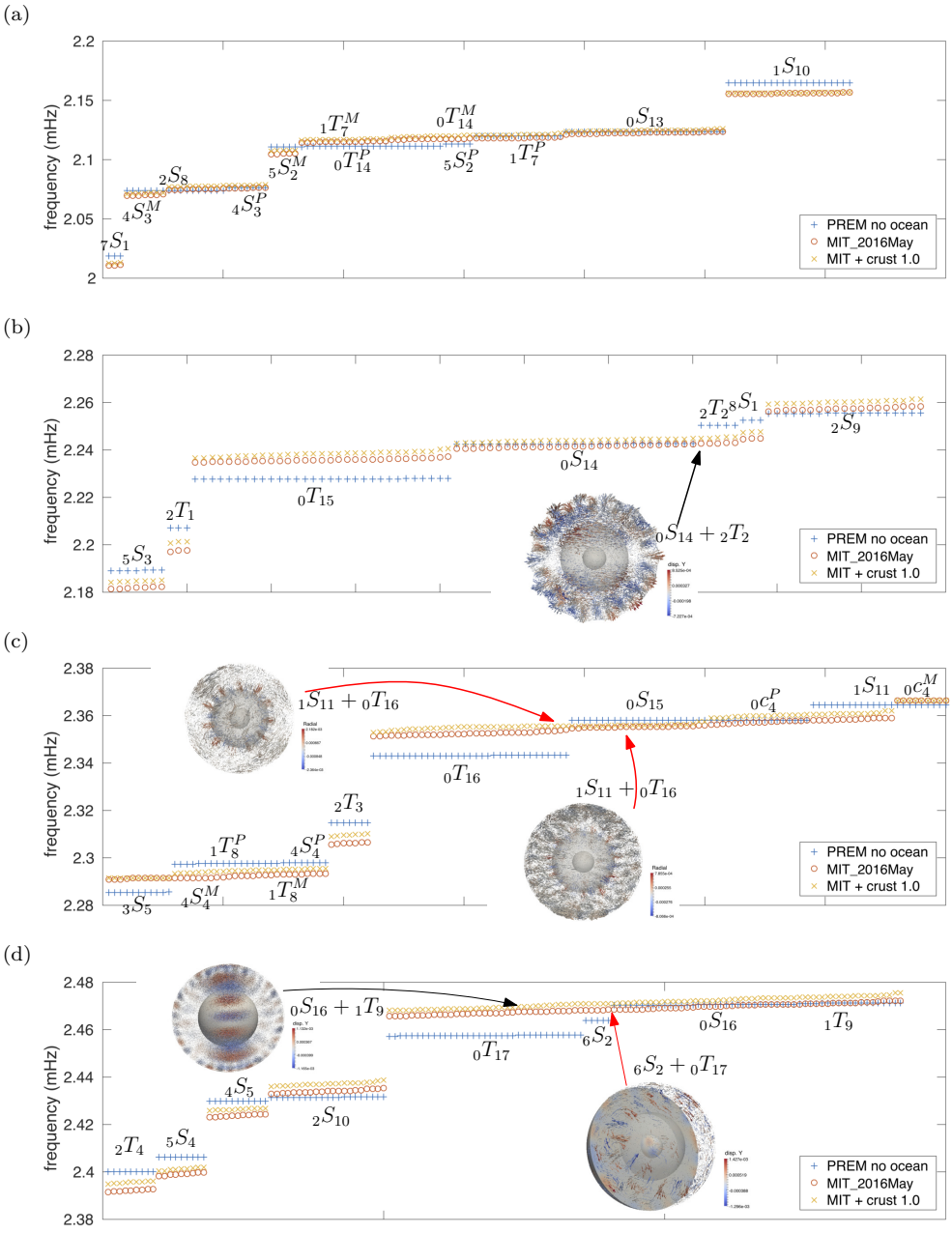

Figure 5. Comparisons amongst different Earth models. The results from PREM without ocean, MIT model, and MIT model with the 3D crust are shown using blue +, red ∘ and yellow ×, respectively. The upper scripts P, M on the mode symbols ($_nS_l$, $_nT_l$) denote PREM and MIT models, respectively. (a-d) Comparison for different modes in $[2.0, 2.18]$, $[2.18, 2.28]$, $[2.28, 2.38]$ and $[2.38, 2.48]$mHz, respectively. The mode in (b) couples $_0S_{14}$ with $_2T_2$. The two modes in (c) couple $_1S_{11}$ with $_0T_{16}$. The left mode in (d) couples $_0S_{16}$ with $_1T_9$. The right mode in (d) couples $_6S_2$ with $_0T_{17}$.

REFERENCES

Akbarashrafi, F., Al-Attar, D., Deuss, A., Trampert, J., & Valentine, A., 2017. Exact free oscillation spectra, splitting functions and the resolvability of Earth's density structure, *Geophysical Journal International*, **213**(1), 58–76.

Al-Attar, D., Woodhouse, J. H., & Deuss, A., 2012. Calculation of normal mode spectra in laterally heterogeneous earth models using an iterative direct solution method, *Geophysical Journal International*, **189**(2), 1038–1046.

Al-Attar, D., Crawford, O., Valentine, A. P., & Trampert, J., 2018. Hamiltons principle and normal mode coupling in an aspherical planet with a fluid core, *Geophysical Journal International*, **214**(1), 485–507.

Anderson, E., Bai, Z., Bischof, C., Blackford, S., Dongarra, J., Du Croz, J., Greenbaum, A., Hammarling, S., McKenney, A., & Sorensen, D., 1999. *LAPACK Users' guide*, vol. 9, SIAM.

Bathe, K.-J., 2006. *Finite element procedures*, Klaus-Jurgen Bathe.

Beghein, C., Resovsky, J., & Van Der Hilst, R. D., 2008. The signal of mantle anisotropy in the coupling of normal modes, *Geophysical Journal International*, **175**(3), 1209–1234.

Bermúdez, A. & Rodríguez, R., 1994. Finite element computation of the vibration modes of a fluid-solid system, *Computer Methods in Applied Mechanics and Engineering*, **119**(3), 355–370.

Bermúdez, A., Durán, R., Muschietti, M., Rodríguez, R., & Solomin, J., 1995. Finite element vibration analysis of fluid-solid systems without spurious modes, *SIAM Journal on Numerical Analysis*, **32**(4), 1280–1295.

Bermúdez, A., Hervella-Nieto, L., & Rodriguez, R., 1999. Finite element computation of three-dimensional elastoacoustic vibrations, *Journal of Sound and Vibration*, **219**(2), 279–306.

Brezzi, F. & Fortin, M., 2012. *Mixed and hybrid finite element methods*, vol. 15, Springer Science & Business Media.

Buland, R. & Gilbert, F., 1984. Computation of free oscillations of the Earth, *Journal of Computational Physics*, **54**(1), 95–114.

Burdick, S., Vernon, F. L., Martynov, V., Eakins, J., Cox, T., Tytell, J., Mulder, T., White, M. C., Astiz, L., Pavlis, G. L., & van der Hilst, R. D., 2017. Model update May 2016: Upper-mantle heterogeneity beneath North America from travel-time tomography with global and USArray data, *Seismological Research Letters*, **88**(2A), 319–325.

Burnett, D. S., 1994. A three-dimensional acoustic infinite element based on a prolate spheroidal multipole expansion, *The Journal of the Acoustical Society of America*, **96**(5), 2798–2816.

Chaljub, E., Capdeville, Y., & Vilotte, J.-P., 2003. Solving elastodynamics in a fluid–solid heterogeneous sphere: a parallel spectral element approximation on non-conforming grids, *Journal of Computational Physics*, **187**(2), 457–491.

Chaljub, E., Komatitsch, D., Vilotte, J.-P., Capdeville, Y., Valette, B., & Festa, G., 2007. Spectral-element analysis in seismology, *Advances in geophysics*, **48**, 365–419.

Chen, H. C. & Taylor, R. L., 1990. Vibration analysis of fluid–solid systems using a finite element displacement formulation, *International Journal for Numerical Methods in Engineering*, **29**(4), 683–698.

Craggs, A., 1971. The transient response of a coupled plate-acoustic system using plate and acoustic finite elements, *Journal of Sound and Vibration*, **15**(4), 509–528.

Dahlen, F. A. & Tromp, J., 1998. *Theoretical global seismology*, Princeton University press.

de Hoop, M. V., Holman, S., & Pham, H., 2015. On the system of elastic-gravitational equations describing the oscillations of the earth, *arXiv preprint arXiv:1511.03200*.

de Hoop, M. V., Holman, S., Jimbo, S., & Nakamura, G., 2019. Characterization of the spectrum of the earth and normal modes, *in preparation*.

Deuss, A. & Woodhouse, J., 2004. Iteration method to determine the eigenvalues and eigenvectors of a target multiplet including full mode coupling, *Geophysical Journal International*, **159**(1), 326–332.

Deuss, A. & Woodhouse, J. H., 2001. Theoretical free-oscillation spectra: the importance of wide band coupling, *Geophysical Journal International*, **146**(3), 833–842.

Ern, A. & Guermond, J.-L., 2013. *Theory and practice of finite elements*, vol. 159, Springer Science & Business Media.

Everstine, G. C., 1981. A symmetric potential formulation for fluid-structure interaction, *Journal of Sound and Vibration*, **79**(1), 157–160.

Fang, H. & Saad, Y., 2012. A Filtered Lanczos Procedure for Extreme and Interior Eigenvalue Problems, *SIAM Journal on Scientific Computing*, **34**(4), A2220–A2246.

Gharti, H. N., Tromp, J., & Zampini, S., 2018. Spectral-infinite-element simulations of gravity anomalies, *Geophysical Journal International*, **215**(2), 1098–1117.

Gimbutas, Z. & Greengard, L., 2011. FMMLIB3D 1.2, FORTRAN libraries for fast multiple method in three dimensions.

Greengard, L. & Rokhlin, V., 1987. A fast algorithm for particle simulations, *Journal of Computational Physics*, **73**(2), 325–348.

Greengard, L. & Rokhlin, V., 1997. A new version of the fast multipole method for the Laplace equation in three dimensions, *Acta numerica*, **6**, 229–269.

Hamdi, M. A., Ousset, Y., & Verchery, G., 1978. A displacement method for the analysis of vibrations of coupled fluid-structure systems, *International Journal for Numerical Methods in Engineering*, **13**(1), 139–150.

Hesthaven, J. S. & Warburton, T., 2007. *Nodal discontinuous Galerkin methods: algorithms, analysis, and applica-*

tions, vol. 54, Springer Science & Business Media.

Hughes, T. J., 2012. *The finite element method: linear static and dynamic finite element analysis*, Courier Corporation.

Irving, J., Deuss, A., & Woodhouse, J., 2009. Normal mode coupling due to hemispherical anisotropic structure in Earth's inner core, *Geophysical Journal International*, **178**(2), 962–975.

Kennett, B., Engdahl, E., & Buland, R., 1995. Constraints on seismic velocities in the earth from traveltimes, *Geophysical Journal International*, **122**(1), 108–124.

Kiefling, L. & Feng, G., 1976. Fluid-structure finite element vibrational analysis, *AIAA Journal*, **14**(2), 199–203.

Koelemeijer, P., Deuss, A., & Trampert, J., 2012. Normal mode sensitivity to Earth's D" layer and topography on the core-mantle boundary: what we can and cannot see, *Geophysical Journal International*, **190**(1), 553–568.

Komatitsch, D. & Tromp, J., 2002. Spectral-element simulations of global seismic wave propagation–II. Three-dimensional models, oceans, rotation and self-gravitation, *Geophysical Journal International*, **150**(1), 303–318.

Laske, G., Masters, G., Ma, Z., & Pasyanos, M., 2013. Update on CRUST1. 0A 1-degree global model of Earths crust, in *Geophys. Res. Abstr*, vol. 15, p. 2658, EGU General Assembly Vienna, Austria.

Li, R., Xi, Y., Vecharynski, E., Yang, C., & Saad, Y., 2016. A Thick-Restart Lanczos algorithm with polynomial filtering for Hermitian eigenvalue problems, *SIAM J. Sci. Comput.*, **38**(4), A2512–A2534.

Li, R., Xi, Y., Erlandson, L., & Saad, Y., 2018. The Eigenvalues Slicing Library (EVSL): Algorithms, Implementation, and Software, *arXiv preprint arXiv:1802.05215*.

Lognonné, P., 2005. Planetary seismology, *Annu. Rev. Earth Planet. Sci.*, **33**, 571–604.

Masters, G., Barmine, M., & Kientz, S., 2011. Mineos: User Manual Version 1.0.2, *Cal Inst of Tech*.

Nader, M., Igel, H., Ferreira, A., Al-Attar, D., Wassermann, J., & Schreiber, K., 2015. Normal mode coupling observations with a rotation sensor, *Geophysical Journal International*, **201**(3), 1482–1490.

Nissen-Meyer, T., Fournier, A., & Dahlen, F., 2008. A 2-D spectral-element method for computing spherical-earth seismograms – II. Waves in solid–fluid media, *Geophysical Journal International*, **174**(3), 873–888.

Olson, L. G. & Bathe, K.-J., 1983. A study of displacement–based fluid finite elements for calculating frequencies of fluid and fluid-structure systems, *Nuclear Engineering and Design*, **76**(2), 137–151.

Olson, L. G. & Bathe, K.-J., 1985. Analysis of fluid-structure interactions. a direct symmetric coupled formulation based on the fluid velocity potential, *Computers & Structures*, **21**(1), 21–32.

Parlett, B. N., 1998. *The Symmetric Eigenvalue Problem*, no. 20 in Classics in Applied Mathematics, SIAM, Philadelphia.

Persson, P.-O. & Strang, G., 2004. A simple mesh generator in MATLAB, *SIAM review*, **46**(2), 329–345.

Romanowicz, B. A., Panning, M. P., Gung, Y., & Capdeville, Y., 2008. On the computation of long period seismograms in a 3-D earth using normal mode based approximations, *Geophysical Journal International*, **175**(2), 520–536.

Saad, Y., 2006. Filtered conjugate residualtype algorithms with applications, *SIAM Journal on Matrix Analysis and Applications*, **28**(3), 845–870.

Shi, J., Li, R., Xi, Y., Saad, Y., & de Hoop, M. V., 2018. Computing planetary interior normal modes with a highly parallel polynomial filtering eigensolver, in *Proceedings of the International Conference for High Performance Computing, Networking, Storage, and Analysis, SC'18, Dallas, TX, USA, November 11-16, 2018*, pp. 71:1–71:13.

Si, H., 2015. TetGen, a Delaunay-based quality tetrahedral mesh generator, *ACM Transactions on Mathematical Software (TOMS)*, **41**(2), 11.

Slichter, L. B., 1961. The Fundamental free mode of the Earth's inner core, *Proceedings of the National Academy of Sciences*, **47**(2), 186–190.

Wang, X. & Bathe, K.-J., 1997. Displacement/pressure based mixed finite element formulations for acoustic fluid-structure interaction problems, *International Journal for Numerical Methods in Engineering*, **40**(11), 2001–2017.

Woodhouse, J., 1980. The coupling and attenuation of nearly resonant multiplets in the earth's free oscillation spectrum, *Geophysical Journal International*, **61**(2), 261–283.

Woodhouse, J., 1988. The calculation of the eigenfrequencies and eigenfunctions of the free oscillations of the Earth and Sun, *Seismological algorithms: computational methods and computer programs*, pp. 321–370.

Woodhouse, J. & Dahlen, F., 1978. The effect of a general aspherical perturbation on the free oscillations of the Earth, *Geophysical Journal of the Royal Astronomical Society*, **53**(2), 335–354.

Woodhouse, J. & Deuss, A., 2007. Theory and observations – Earth's free oscillations, *Seismology and Structure of the Earth: Treatise on Geophysics*, **1**, 31–65.

Yang, H.-Y. & Tromp, J., 2015. Synthetic free-oscillation spectra: an appraisal of various mode-coupling methods, *Geophysical Journal International*, **203**(2), 1179–1192.

Ye, J., 2018. *Revisiting the computation of normal modes in SNREI models of planets – close eigenfrequencies*, Master's thesis, Rice University.

Yokota, R., 2013. An FMM based on dual tree traversal for many-core architectures, *Journal of Algorithms & Computational Technology*, **7**(3), 301–324.

Zienkiewicz, O. & Bettess, P., 1978. Fluid-structure dynamic interaction and wave forces. An introduction to numerical treatment, *International Journal for Numerical Methods in Engineering*, **13**(1), 1–16.

Zienkiewicz, O., Emson, C., & Bettess, P., 1983. A novel boundary infinite element, *International Journal for*

Numerical Methods in Engineering, **19**(3), 393–404.
Zienkiewicz, O. C. & Newton, R. E., 1969. *Coupled vibrations of a structure submerged in a compressible fluid*.
Zienkiewicz, O. C. & Taylor, R. L., 2005. *The finite element method for solid and structural mechanics*, Elsevier.

APPENDIX A: FULL MODE COUPLING

Concerning the Galerkin approximation, we may use different bases of functions in the appropriate energy space. In this appendix, we consider the use of eigenfunctions of a spherically symmetric, non-rotating, perfectly elastic and isotropic (SNREI) reference model as a basis. This was proposed by Woodhouse & Dahlen (1978); Woodhouse (1980); Deuss & Woodhouse (2001, 2004). An immediate drawback of using this basis, however, is that the fluid-solid boundaries need to be spherically symmetric as these are encoded in these basis functions.

We let u_{km} represent the eigenfunctions associated with eigenfrequencies, ω_k, in terms of spherical harmonics, Y_l^m, that is,

$$u_{km} = U_{km}\mathbf{P}_{lm} + V_{km}\mathbf{B}_{lm} + W_{km}\mathbf{C}_{lm} \quad \text{(no summation over } m\text{)},$$

where k is the multi-index for the eigenfrequency; $m = -l, -l+1 \ldots, l-1, l$ is the index corresponding with the degeneracy with l denoting the spherical harmonic degree; U_{km}, V_{km} and W_{km} are the three components of eigenfunctions and are functions of the radial coordinate; $\mathbf{P}_{lm}$, $\mathbf{B}_{lm}$ and $\mathbf{C}_{lm}$ are the vector spherical harmonics, see (Dahlen & Tromp 1998, (8.36)) for their definition. In addition, p_{km} needs to be introduced to constrain the solution, cf. (13) (de Hoop et al. 2019, Subsection 3.3). Since $\nabla \cdot u_{km}(x)$ can be expended using $Y_l^m(x)$ (Dahlen & Tromp 1998, (8.38)) and $u_{km}(x) \cdot g_{(r)}$ can also be expended using $Y_l^m(x)$ for the radial models, we let $p_{km} = P_{km}Y_l^m$ with

$$P_{km} = -\kappa_{(r)}\left[\partial_r U_{km} + r^{-1}(2U_{km} - \sqrt{l(l+1)}V_{km})\right] + \rho^0_{(r)}g_{(r)}U_{km},$$

where $\rho^0_{(r)}$, $\kappa_{(r)}$ and $g_{(r)}$ denote the radial profiles of the density, bulk modulus and reference gravitational field of a radial model, respectively. Similarly, the incremental gravitational potential of the radial models takes the form, $s_{km} = S_{km}Y_l^m$, where S_{km} is also a function in the radial coordinate. In the following, l and m are fixed.

In an SNREI model, for the computation of the toroidal modes, we only need to consider a solid annulus comprising the mantle and the crust. We exemplify the computations with the spheroidal modes and let U'_{km}, P'_{km} and S'_{km} be test functions for U_{km}, P_{km} and S_{km} following the Galerkin method. We let the $\tilde{X}_{(r)}$ be the 1D interval of the radial planet and have $\tilde{X}_{(r)} = \Omega^{\mathrm{S}}_{(r)} \cup \Omega^{\mathrm{F}}_{(r)}$, where $\Omega^{\mathrm{S}}_{(r)}$ and $\Omega^{\mathrm{F}}_{(r)}$ denote the 1D intervals for the solid and fluid regions, respectively. Given a regular finite-element partitioning $\mathcal{T}_h^{(r)}$ of the interval $\tilde{X}_{(r)}$, we denote an element of the mesh by $L_q \in \mathcal{T}_h^{(r)}$ and have $\tilde{X}_{(r)} = \bigcup_{q=1}^{N_L} L_q$, where N_L denotes the total number of 1D elements. Furthermore, we let L_q^{S} and L_q^{F} specifically be elements in the solid and fluid regions and have

$$\Omega^{\mathrm{S}}_{(r)} = \bigcup_{q=1}^{N_L^{\mathrm{S}}} L_q^{\mathrm{S}}, \quad \Omega^{\mathrm{F}}_{(r)} = \bigcup_{q=1}^{N_L^{\mathrm{F}}} L_q^{\mathrm{F}},$$

where N_L^{S} and N_L^{F} denote the numbers of 1D elements in the solid and fluid regions, respectively. We let $\Sigma^{\mathrm{FS}}_{(r)}$ denote the fluid-solid boundary points in the radial interval. We introduce the finite-element solutions, $U^s_{km;h}$, $U^f_{km;h}$, $V^s_{km;h}$, $V^f_{km;h}$, $P_{km;h}$ and $S_{km;h}$, and test functions, $U^{s'}_{km;h}$, $U^{f'}_{km;h}$, $V^{s'}_{km;h}$, $V^{f'}_{km;h}$, $P'_{km;h}$ and $S'_{km;h}$. We set $N_{p^U} = (p^U + 1)/2$, where N_{p^U} is the number of nodes on a 1D element for the p^U-th order polynomial approximation. We have likewise expressions for N_{p^V}, N_{p^P} and N_{p^S}. Similar to Subsection 3.3, we introduce nodal based Lagrange polynomials, ℓ_i^U, ℓ_i^V, ℓ_i^P, ℓ_i^S, on the resepctive 1D elements $L \in \mathcal{T}_h^{(r)}$,

and write

$$U^s_{km;h}(x) = \sum_{i=1}^{N_{pU}} U^s_{km;h}(x_i)\ell^U_i(x), \quad U^f_{km;h}(x) = \sum_{i=1}^{N_{pU}} U^f_{km;h}(x_i)\ell^U_i(x), \tag{A.1}$$

$$V^s_{km;h}(x) = \sum_{i=1}^{N_{pV}} V^s_{km;h}(x_i)\ell^V_i(x), \quad V^f_{km;h}(x) = \sum_{i=1}^{N_{pV}} V^f_{km;h}(x_i)\ell^V_i(x), \tag{A.2}$$

$$P_{km}(x) = \sum_{i=1}^{N_{pP}} P_{km}(x_i)\ell^P_i(x), \quad S_{km}(x) = \sum_{i=1}^{N_{pS}} S_{km}(x_i)\ell^S_i(x), \tag{A.3}$$

for $x \in L^{\mathrm{S}}$ and $x \in L^{\mathrm{F}}$, respectively; similar representations hold for $U^{s'}_{km;h}$, $U^{f'}_{km;h}$, $V^{s'}_{km;h}$, $V^{f'}_{km;h}$, $P'_{km;h}$ and $S'_{km;h}$, respectively. We note that the fluid-solid boundary points coincide with nodes.

Similarly to Subsection 3.4 and Section 4, we collect the "values" of $U^s_{km;h}$, $U^f_{km;h}$, $V^s_{km;h}$, $V^f_{km;h}$, $P_{km;h}$ and $S_{km;h}$ at all the nodes, in vectors $\tilde{U}^s_{km}$, $\tilde{U}^f_{km}$, $\tilde{V}^s_{km}$, $\tilde{V}^f_{km}$, $\tilde{V}_{km}$ and $\tilde{S}_{km}$, respectively, and collect the values of $U^{s'}_{km;h}$, $U^{f'}_{km;h}$, $V^{s'}_{km;h}$, $V^{f'}_{km;h}$, $P'_{km;h}$ and $S'_{km;h}$ at all the nodes, in "vectors" $\tilde{U}^{s'}_{km}$, $\tilde{U}^{f'}_{km}$, $\tilde{V}^{s'}_{km}$, $\tilde{V}^{f'}_{km}$, $\tilde{P}'_{km}$ and $\tilde{S}'_{km}$, respectively. We let

$$\tilde{u}^{(r)}_{km} = ((\tilde{U}^s_{km})^{\mathsf{T}}, (\tilde{V}^s_{km})^{\mathsf{T}}, (\tilde{U}^f_{km})^{\mathsf{T}}, (\tilde{V}^f_{km})^{\mathsf{T}})^{\mathsf{T}},$$
$$\tilde{u}^s_{km} = ((\tilde{U}^s_{km})^{\mathsf{T}}, (\tilde{V}^s_{km})^{\mathsf{T}})^{\mathsf{T}}, \quad \tilde{u}^f_{km} = ((\tilde{U}^f_{km})^{\mathsf{T}}, (\tilde{V}^f_{km})^{\mathsf{T}})^{\mathsf{T}},$$

and obtain the resulting eigenvalue problem (cf. (64))

$$(A^{(r)}_G - E^{(r)}_G {A^{(r)}_p}^{-1} {E^{(r)}_G}^{\mathsf{T}} - {C^{(r)}}^{\mathsf{T}}(S^{(r)})^{-1}C^{(r)})\tilde{u}^{(r)}_{km} = \omega^2_k M^{(r)}\tilde{u}^{(r)}_{km}, \tag{A.4}$$

where

$$A^{(r)}_G = \begin{pmatrix} A^{(r)}_{sg} & 0 \\ 0 & A^{(r)}_f \end{pmatrix}, \; E^{(r)}_G = \begin{pmatrix} E^{(r)}_{\mathrm{FS}} \\ A^{(r)}_{\mathrm{dg}} \end{pmatrix}, \; {C^{(r)}}^{\mathsf{T}} = \begin{pmatrix} {C^{(r)}_s}^{\mathsf{T}} \\ {C^{(r)}_f}^{\mathsf{T}} \end{pmatrix},$$
$$M^{(r)} = \begin{pmatrix} M^{(r)}_s & 0 \\ 0 & M^{(r)}_f \end{pmatrix}, \; {E^{(r)}_G}^{\mathsf{T}} = \begin{pmatrix} {E^{(r)}_{\mathrm{FS}}}^{\mathsf{T}} & {A^{(r)}_{\mathrm{dg}}}^{\mathsf{T}} \end{pmatrix}, \; C^{(r)} = \begin{pmatrix} C^{(r)}_s & C^{(r)}_f \end{pmatrix},$$

in which $A^{(r)}_{sg}$, $A^{(r)}_f$, $A^{(r)}_p$, $E^{(r)}_{\mathrm{FS}}$, ${E^{(r)}_{\mathrm{FS}}}^{\mathsf{T}}$, $A^{(r)}_{\mathrm{dg}}$, ${A^{(r)}_{\mathrm{dg}}}^{\mathsf{T}}$, $M^{(r)}_s$, $M^{(r)}_f$, ${C^{(r)}_s}^{\mathsf{T}}$, ${C^{(r)}_f}^{\mathsf{T}}$, $S^{(r)}$, $C^{(r)}_s$ and $C^{(r)}_f$, are given in Tables A.1 and A.2. We note that the matrices in (A.4) are obtained using separation of variables with spherical harmonics in (64); We substitute

$$\tilde{P}_{km} = -{A^{(r)}_p}^{-1}{E^{(r)}_G}^{\mathsf{T}}\tilde{u}^{(r)}_{km}$$

upon solving (16) and

$$\tilde{S}_{km} = (S^{(r)})^{-1}C^{(r)}\tilde{u}^{(r)}_{km}$$

upon solving (2). We only need to invoke a finite-element basis in the radial coordinate. We note that the resulting system can be solved via a standard eigensolver, such as `LAPACK` (Anderson et al. 1999).

As mentioned above, we may consider the finite-element solution denoted as $\{u_{km;h}\}$ as an alternative basis. Since $\{u_{km;h}\}$ is a global basis for the general problem, we have no separation in the solid and fluid components and no longer have the fluid-solid boundary terms in the system. Following the Galerkin method, we then consider an expansion for the general solution $u_c = \sum_{km} y_{km}u_{km;h}$ and the corresponding test functions $v_c = \sum_{k'm'} y'_{k'm'}u_{k'm';h}$. We introduce s_c and their corresponding test functions v^{s_c} for self-gravitation. We have $s_c = \sum_{km} z_{km}S_{km;h}$ and $v^{s_c} = \sum_{k'm'} z'_{k'm'}S_{k'm';h}$. Assuming that all the discontinuities in a fully heterogeneous model coincide with the ones in the reference radial model and the fluid outer core, the eigenfuncions represented by the mentioned expansions lie in $H_1 \subset E$ (cf. (10)) for the fully heterogeneous problem while the constraint equation disappears. We let y, y', z and z' be the "vectors" with components y_{km}, $y'_{k'm'}$, z_{km} and $z'_{k'm'}$, respectively, and obtain

$$(A^{(c)}_G - {C^{(c)}}^{\mathsf{T}}{S^{(c)}}^{-1}C^{(c)})y = \omega^2 M^{(c)}y, \tag{A.5}$$

as the counterpart of (64). Here, $A^{(c)}_G$, $M^{(c)}$, ${C^{(c)}}^{\mathsf{T}}$, $S^{(c)}$ and $C^{(c)}$ obtained via substituting the above-mentioned expansion of u_c in (64), are given in Tables A.3 and A.4.

operations	physical relations	corresponding formulae
$(\tilde{U}^{s'}_{km})^{\mathsf{T}} A^{(r)}_{sg} \tilde{U}^{s}_{km}$	solid stiffness matrix	(Ye 2018, (3.1))
$(\tilde{U}^{f'}_{km})^{\mathsf{T}} A^{(r)}_{f} \tilde{U}^{f}_{km}$	Brunt-Väisälä frequency	$\int_{\Omega^{\mathrm{F}}_{(r)}} U^{f'}_{km;h} U^{f}_{km;h} N^2_{(r)} \rho^0_{(r)} r^2 \,\mathrm{d}r$
$(\tilde{P}'_{km})^{\mathsf{T}} A^{(r)}_{p} \tilde{P}_{km}$	fluid potential	$\int_{\Omega^{\mathrm{F}}_{(r)}} P'_{km;h} P_{km;h} \kappa^{-1}_{(r)} r^2 \,\mathrm{d}r$
$(\tilde{u}^{f'}_{km})^{\mathsf{T}} A^{(r)}_{\mathrm{dg}} \tilde{P}_{km}$	fluid stiffness matrix	$\int_{\Omega^{\mathrm{F}}_{(r)}} U^{f'}_{km;h} (\partial_r P_{km;h} + \rho^0_{(r)} g_{(r)} \kappa^{-1}_{(r)} P_{km;h}) r^2 \,\mathrm{d}r$ $+ \int_{\Omega^{\mathrm{F}}_{(r)}} \sqrt{l(l+1)} P_{km;h} V^{f'}_{km;h} r \,\mathrm{d}r$
$(\tilde{P}'_{km})^{\mathsf{T}} A^{(r)\mathsf{T}}_{\mathrm{dg}} \tilde{u}^{f}_{km}$	constraint	$\int_{\Omega^{\mathrm{F}}_{(r)}} \left(\partial_r P'_{km;h} + \rho^0_{(r)} g_{(r)} \kappa^{-1}_{(r)} P'_{km;h}\right) U^{f}_{km;h} r^2 \,\mathrm{d}r$ $+ \int_{\Omega^{\mathrm{F}}_{(r)}} \sqrt{l(l+1)} P'_{km;h} V^{f}_{km;h} r \,\mathrm{d}r$
$(\tilde{U}^{s'}_{km})^{\mathsf{T}} E^{(r)}_{\mathrm{FS}} \tilde{P}_{km}$	fluid-solid boundary condition	$-P_{km;h} U^{s'}_{km;h} r^2 \vert_{\Sigma^{\mathrm{FS}}_{(r)}}$
$(\tilde{P}'_{km})^{\mathsf{T}} E^{(r)\mathsf{T}}_{\mathrm{FS}} \tilde{U}^{s}_{km}$	fluid-solid boundary condition	$-P'_{km;h} U^{s}_{km;h} r^2 \vert_{\Sigma^{\mathrm{FS}}_{(r)}}$
$(\tilde{U}^{s'}_{km})^{\mathsf{T}} M^{(r)}_{s} \tilde{U}^{s}_{km}$	solid mass matrix	$\int_{\Omega^{\mathrm{S}}_{(r)}} \left(U^{s'}_{km;h} U^{s}_{km;h} + V^{s'}_{km;h} V^{s}_{km;h}\right) \rho^0_{(r)} r^2 \,\mathrm{d}r$
$(\tilde{U}^{f'}_{km})^{\mathsf{T}} M^{(r)}_{f} \tilde{U}^{f}_{km}$	fluid mass matrix	$\int_{\Omega^{\mathrm{F}}_{(r)}} \left(U^{f'}_{km;h} U^{f}_{km;h} + V^{f'}_{km;h} V^{f}_{km;h}\right) \rho^0_{(r)} r^2 \,\mathrm{d}r$

Table A.1. Implicit definition of the matrices in (A.4) (no summations over k and m). Since the construction of $A^{(r)}_{sg}$ is standard, we refer to (Dahlen & Tromp 1998, (8.43) & (8.44)) and (Ye 2018, (3.1)). In the above, $\int_{\Omega^{\mathrm{S}}_{(r)}} = \sum_{q=1}^{N^{\mathrm{S}}_L} \int_{L^{\mathrm{S}}_q}$ and $\int_{\Omega^{\mathrm{F}}_{(r)}} = \sum_{q=1}^{N^{\mathrm{F}}_L} \int_{L^{\mathrm{F}}_q}$.

operations	physical relations	corresponding formulae
$(\tilde{S}'_{km})^{\mathsf{T}} C^{(r)}_{s} \tilde{u}^{s}_{km}$	density changes in $\overline{\Omega^{\mathrm{S}}_{(r)}}$	$\int_{\Omega^{\mathrm{S}}_{(r)}} (\partial_r S'_{km;h}) U^{s}_{km;h} \rho^0_{(r)} r^2 \,\mathrm{d}r$ $+ \int_{\Omega^{\mathrm{S}}_{(r)}} \sqrt{l(l+1)} S'_{km;h} V^{s}_{km;h} \rho^0_{(r)} r \,\mathrm{d}r$
$(\tilde{S}'_{km})^{\mathsf{T}} C^{(r)}_{f} \tilde{u}^{f}_{km}$	density changes in $\overline{\Omega^{\mathrm{F}}_{(r)}}$	$\int_{\Omega^{\mathrm{F}}_{(r)}} (\partial_r S'_{km;h}) U^{f}_{km;h} \rho^0_{(r)} r^2 \,\mathrm{d}r$ $+ \int_{\Omega^{\mathrm{F}}_{(r)}} \sqrt{l(l+1)} S'_{km;h} V^{f}_{km;h} \rho^0_{(r)} r \,\mathrm{d}r$
$(\tilde{S}'_{km})^{\mathsf{T}} S^{(r)} \tilde{S}_{km}$	Poisson's equation	$(4\pi G)^{-1} \int_0^{\infty} (\partial_r S'_{km;h} \partial_r S_{km;h} r^2$ $+ l(l+1) S'_{km;h} S_{km;h}) \,\mathrm{d}r$
$(\tilde{u}^{s'}_{km})^{\mathsf{T}} C^{(r)\mathsf{T}}_{s} \tilde{S}_{km}$	incremental gravitational field in $\overline{\Omega^{\mathrm{S}}_{(r)}}$	$\int_{\Omega^{\mathrm{S}}_{(r)}} U^{s'}_{km;h} (\partial_r S_{km;h}) \rho^0_{(r)} r^2 \,\mathrm{d}r$ $+ \int_{\Omega^{\mathrm{S}}_{(r)}} \sqrt{l(l+1)} V^{s'}_{km;h} S_{km;h} \rho^0_{(r)} r \,\mathrm{d}r$
$(\tilde{u}^{f'}_{km})^{\mathsf{T}} C^{(r)\mathsf{T}}_{f} \tilde{S}_{km}$	incremental gravitational field in $\overline{\Omega^{\mathrm{F}}_{(r)}}$	$\int_{\Omega^{\mathrm{F}}_{(r)}} U^{f'}_{km;h} (\partial_r S_{km;h}) \rho^0_{(r)} r^2 \,\mathrm{d}r$ $+ \int_{\Omega^{\mathrm{F}}_{(r)}} \sqrt{l(l+1)} V^{f'}_{km;h} S_{km;h} \rho^0_{(r)} r \,\mathrm{d}r$

Table A.2. Implicit definition of the matrices in (A.4) (no summation over k and m). In the above, $\int_{\Omega^{\mathrm{S}}_{(r)}} = \sum_{q=1}^{N^{\mathrm{S}}_L} \int_{L^{\mathrm{S}}_q}$ and $\int_{\Omega^{\mathrm{F}}_{(r)}} = \sum_{q=1}^{N^{\mathrm{F}}_L} \int_{L^{\mathrm{F}}_q}$. In the Poisson's equation, the computation of the integral $\int_0^{\infty}$ requires special treatment, see (Ye 2018, Chapter 3.2.2).

operations	physical relations	corresponding formulae
$(y')^{\mathsf{T}} A_G^{(c)} y$	stiffness matrix	$\sum_{km}\sum_{k'm'} y'_{k'm'}\Big\{ \int_{\Omega^{\mathrm{S}}} \nabla u_{k'm';h} : \big(c : \nabla u_{km;h}\big)\ \mathrm{d}x + \int_{\Sigma^{\mathrm{FS}}} \mathfrak{S}\Big\{ \big(g\cdot u_{k'm';h}\big)\ \Big(\nu^{s\to f}\cdot u_{km;h}\Big)\ [\rho^0]^f \Big\}\ \mathrm{d}\Sigma + \int_{\Omega^{\mathrm{S}}} \mathfrak{S}\Big\{ \big(\nabla\cdot u_{k'm';h}\big)\ \big(\rho^0 u_{km;h}\cdot g\big) - \rho^0 u_{k'm';h}\cdot(\nabla g)\cdot u_{km;h} - \rho^0 u_{km;h}\cdot\big(\nabla u_{k'm';h}\big)\cdot g \Big\}\mathrm{d}x + \int_{\Omega^{\mathrm{F}}} \rho^0 N^2\,\frac{\big(g\cdot u_{k'm';h}\big)\ \big(g\cdot u_{km;h}\big)}{\|g\|^2}\,\mathrm{d}x + \int_{\Omega^{\mathrm{F}}} \kappa\,\big(\nabla u_{k'm';h} + \rho^0\kappa^{-1} u_{k'm';h}\cdot g\big)\ \big(\nabla u_{km;h} + \rho^0\kappa^{-1} u_{km;h}\cdot g\big)\ \mathrm{d}x\Big\} y_{km}$
$(y')^{\mathsf{T}} M^{(c)} y$	mass matrix	$\sum_{km}\sum_{k'm'} y'_{k'm'}\Big\{ \int_{\Omega^{\mathrm{S}}} u_{k'm';h}\cdot u_{km;h}\rho^0\,\mathrm{d}x + \int_{\Omega^{\mathrm{F}}} u_{k'm';h}\cdot u_{km;h}\rho^0\,\mathrm{d}x\Big\} y_{km}$

Table A.3. Implicit definition of the matrices in (A.5).

If all the discontinuities in a fully heterogeneous model with a fixed fluid outer core coincide with the reference radial model, we note that the matrix elements in (A.5), Tables A.3 and A.4 are similar to (Woodhouse 1980, (A1)), which describe mode coupling in non-radial models. However, (Woodhouse 1980, (A1)) includes additional terms accounting for changes in the fluid-solid boundaries; this violates the condition that normal modes need to remain in E and in H_1.

operations	physical relations	corresponding formulae
$(z')^{\mathsf{T}} C^{(c)} y$	density changes in $\tilde{X}$	$\sum_{km}\sum_{k'm'} z'_{k'm'}\Big\{ \int_{\Sigma^{\mathrm{SS}}\cup\partial\tilde{X}^{\mathrm{S}}} s_{k'm';h}\nu\cdot u_{km;h}\,\big[\rho^0\big]^+_-\,\mathrm{d}\Sigma + \int_{\Omega^{\mathrm{S}}} s_{k'm';h}\nabla\cdot\big(\rho^0 u_{km;h}\big)\,\mathrm{d}x + \int_{\Sigma^{\mathrm{FS}}} s_{k'm';h}\nu^{f\to s}\cdot u_{km;h}\,\big[\rho^0\big]^s\,\mathrm{d}\Sigma + \int_{\Sigma^{\mathrm{FF}}\cup\partial\tilde{X}^{\mathrm{F}}} s_{k'm';h}\nu\cdot u_{km;h}\,\big[\rho^0\big]^+_-\,\mathrm{d}\Sigma + \int_{\Omega^{\mathrm{F}}} s_{k'm';h}\nabla\cdot(\rho^0 u_{km;h})\,\mathrm{d}x + \int_{\Sigma^{\mathrm{FS}}} s_{k'm';h}\nu^{s\to f}\cdot u_{km;h}\,\big[\rho^0\big]^f\,\mathrm{d}\Sigma\Big\} y_{km}$
$(z')^{\mathsf{T}} S^{(c)} z$	Poisson's equation	$\sum_{km}\sum_{k'm'} z'_{k'm'}\Big\{ \int_{\mathbb{R}^3} (\nabla s_{k'm';h})\cdot(\nabla s_{km;h})\,\mathrm{d}x\Big\} z_{km}$
$(y')^{\mathsf{T}} C^{(c)^{\mathsf{T}}} z$	incremental gravitational field in $\tilde{X}$	$\sum_{km}\sum_{k'm'} y'_{k'm'}\Big\{ \int_{\Sigma^{\mathrm{SS}}\cup\partial\tilde{X}^{\mathrm{S}}} [\rho^0]^+_-\nu\cdot u_{k'm';h} s_{km;h}\,\mathrm{d}\Sigma + \int_{\Omega^{\mathrm{S}}} \nabla\cdot(\rho^0 u_{k'm';h}) s_{km;h}\,\mathrm{d}x + \int_{\Sigma^{\mathrm{FS}}} [\rho^0]^s\nu^{f\to s}\cdot u_{k'm';h} s_{km;h}\,\mathrm{d}\Sigma + \int_{\Sigma^{\mathrm{FF}}\cup\partial\tilde{X}^{\mathrm{F}}} [\rho^0]^+_-\nu\cdot u_{k'm';h} s_{km;h}\,\mathrm{d}\Sigma + \int_{\Omega^{\mathrm{F}}} \nabla\cdot(\rho^0 u_{k'm';h}) s_{km;h}\,\mathrm{d}x + \int_{\Sigma^{\mathrm{FS}}} [\rho^0]^f\nu^{s\to f}\cdot u_{k'm';h} s_{km;h}\,\mathrm{d}\Sigma\Big\} z_{km}$

Table A.4. Implicit definition of the matrices in (A.5).

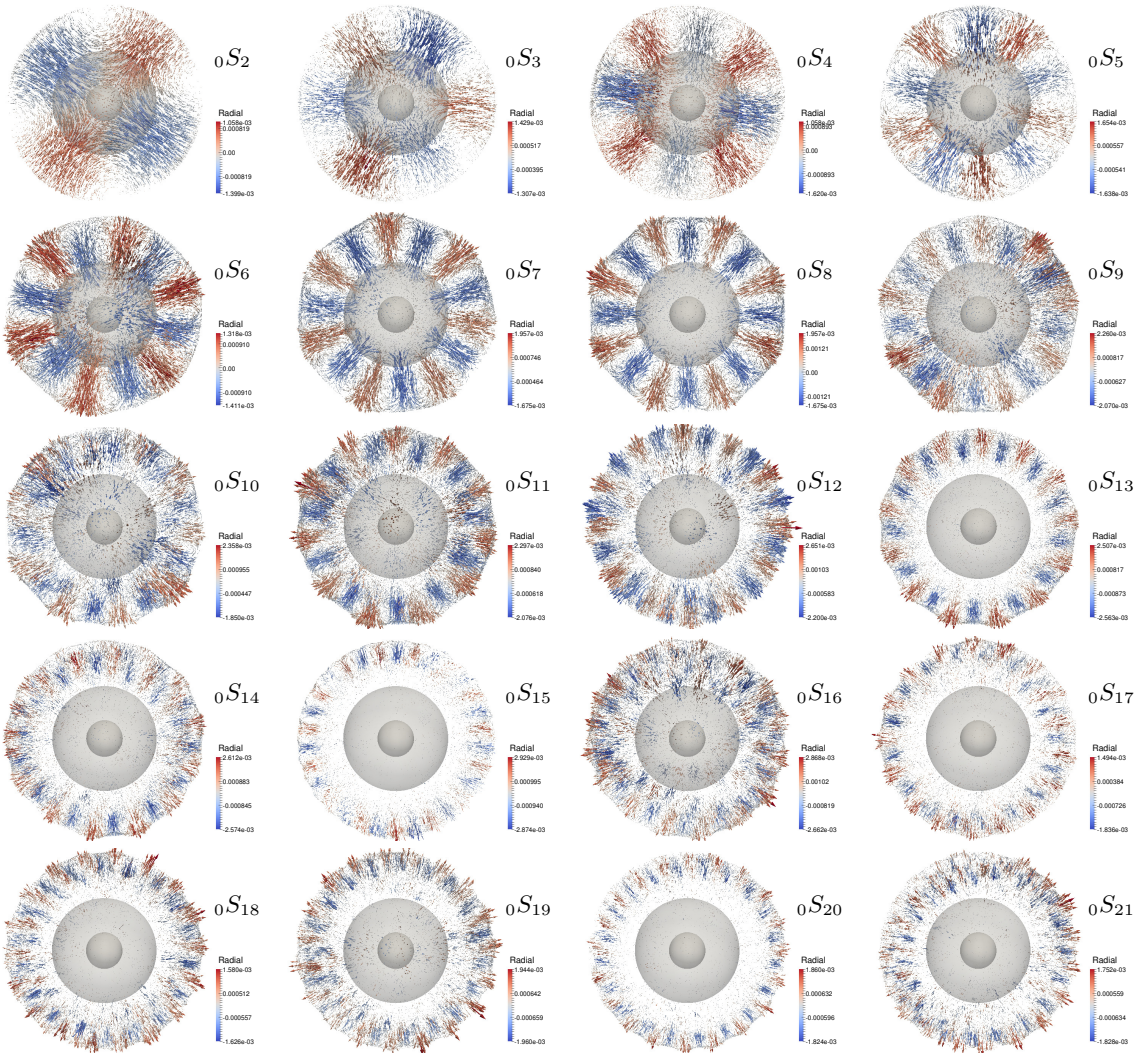

Figure B.1. Illustration of different spheroidal modes with $n = 0$.

APPENDIX B: VISUALIZATION OF NORMAL MODES OF PREM

In this appendix, to gain some insight in their properties, we illustrate the spheroidal and toroidal modes computed in PREM in Figs. B.1 to B.5 and Figs. B.6 to B.8, respectively. The sizes of the arrows indicate the magnitudes of the scaled displacements and the color denote the x, y or radial component. The scaling factor is the square root of the diagonal of the mass matrix M in (72). The visualization is based on around 50,000 evenly distributed displacement vectors on vertices of the finite-element partition $\mathcal{T}_h$.

In Figs. B.1 to B.5, we illustrate spheroidal modes with radial orders $n = 0, 1, 2, 3-6, 7-8$, respectively. In Figs. B.6 to B.8, we show toroidal modes with radial orders $n = 0, 1, 2-3$, respectively. We note that $_1S_1$ is the Slichter mode (Slichter 1961); $_2S_2$, $_3S_3$, $_3S_4$, $_3S_5$, $_4S_6$, $_4S_7$, and $_4S_8$ are ICB Stoneley modes; $_6S_1$, $_6S_2$ and $_7S_3$ are inner core modes.

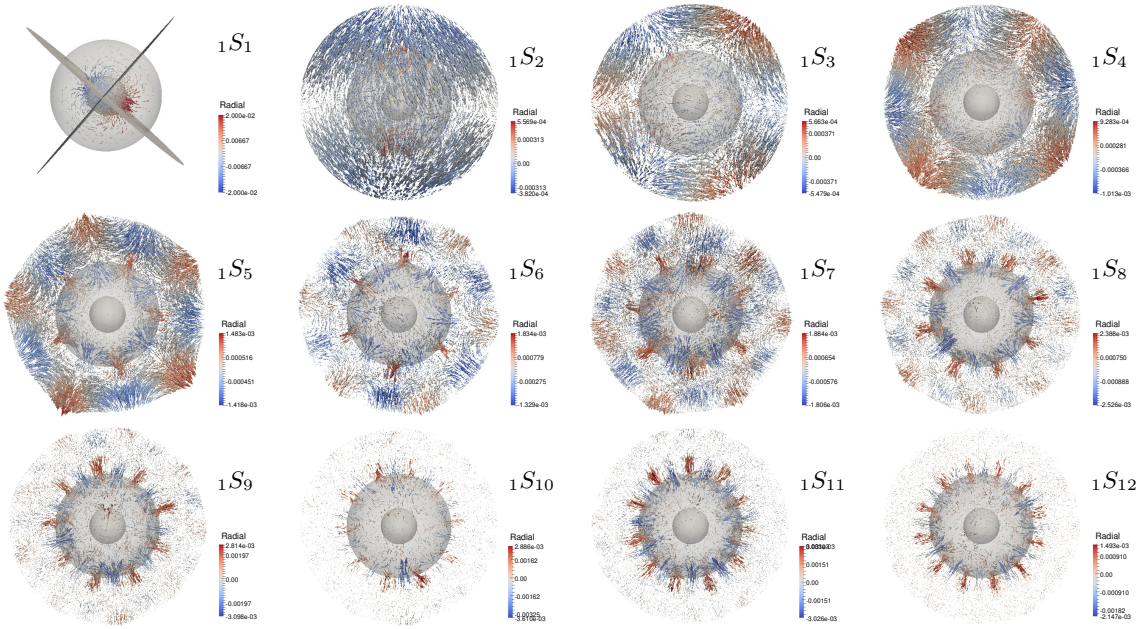

Figure B.2. Illustration of different spheroidal modes with $n = 1$. $_1S_1$ is the Slichter mode.

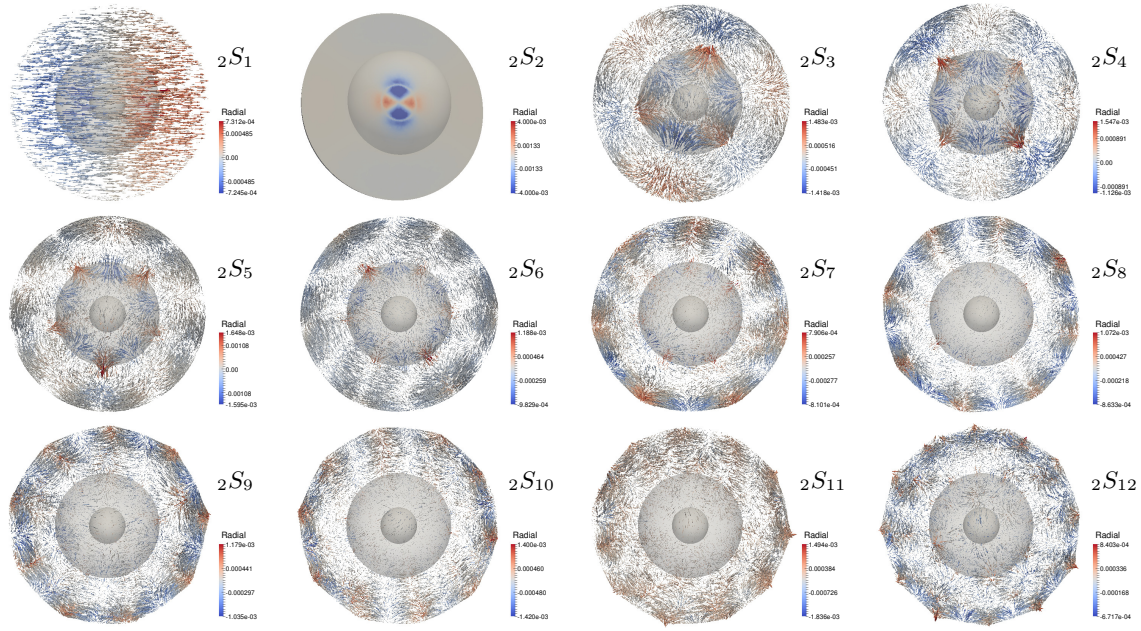

Figure B.3. Illustration of different spheroidal modes with $n = 2$. Note that $_2S_2$ is an ICB Stoneley mode.

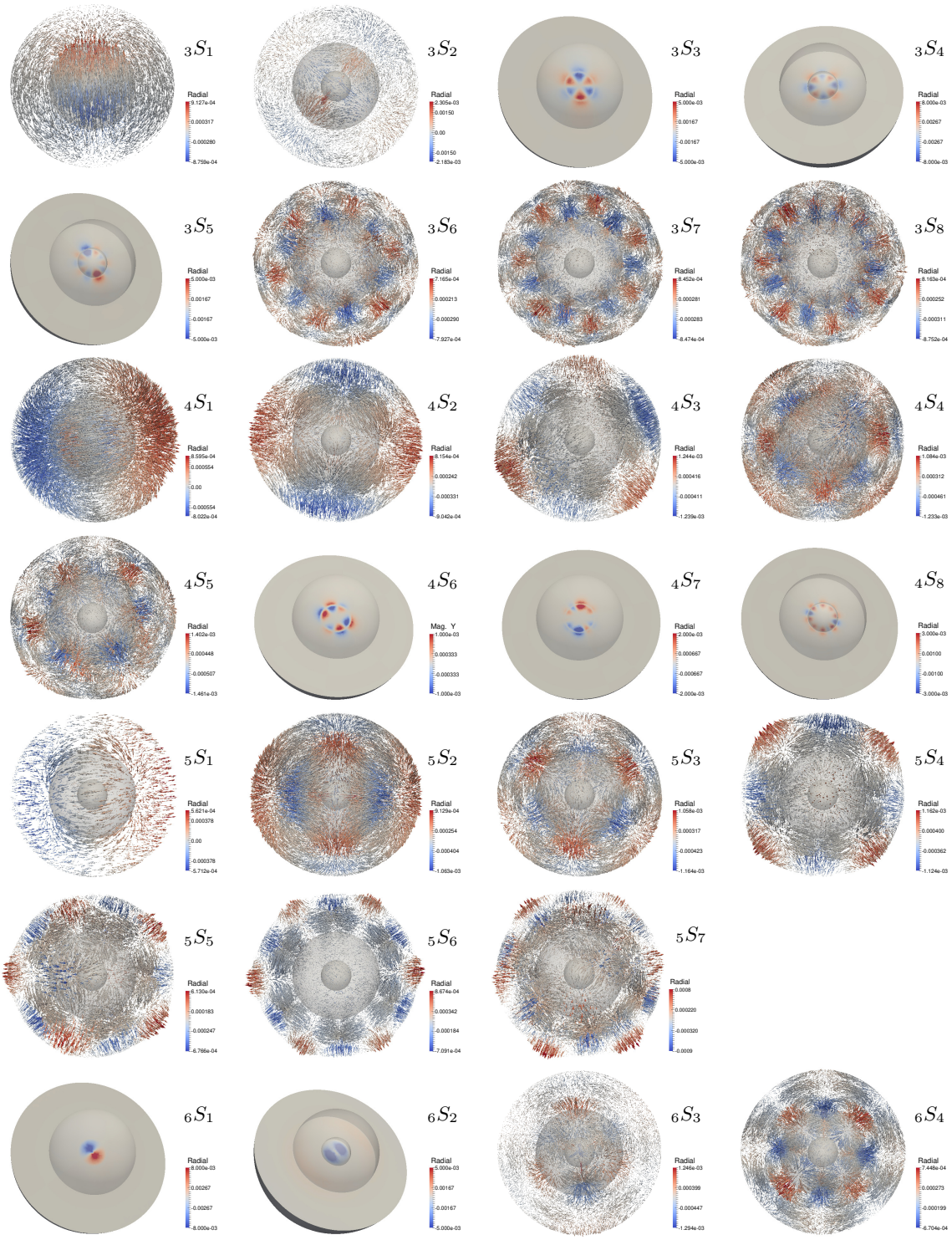

Figure B.4. Illustration of different spheroidal modes with $n = 3, \ldots, 6$. Note that $_3S_3$, $_3S_4$, $_3S_5$, $_4S_6$, $_4S_7$ and $_4S_8$ are ICB Stoneley modes. $_6S_1$ and $_6S_2$ are inner core modes.

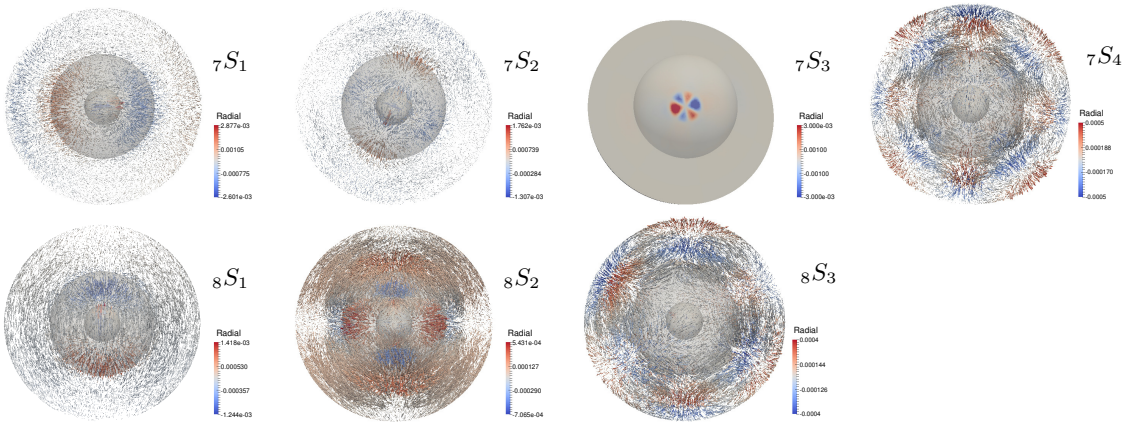

Figure B.5. Illustration of different spheroidal modes with $n = 7, 8$. Note that $_7S_3$ is an inner core mode.

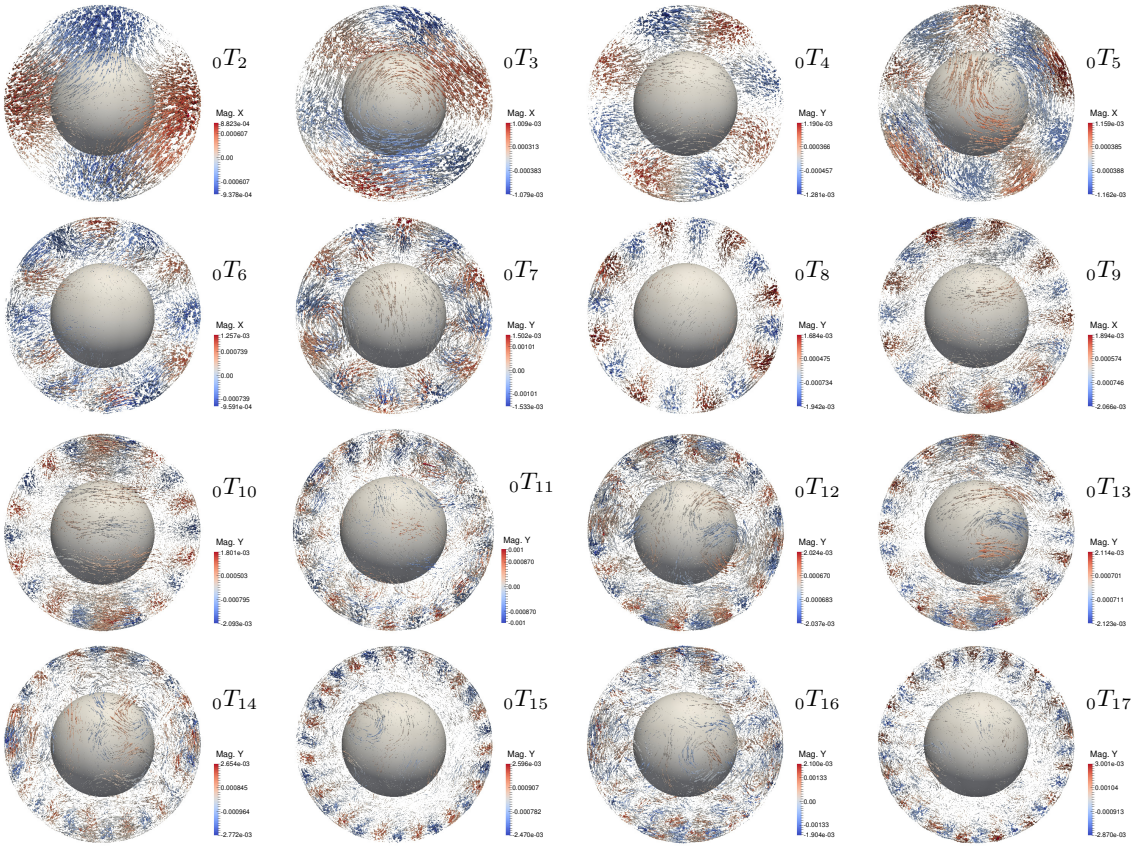

Figure B.6. Illustration of different toroidal modes with $n = 0$.

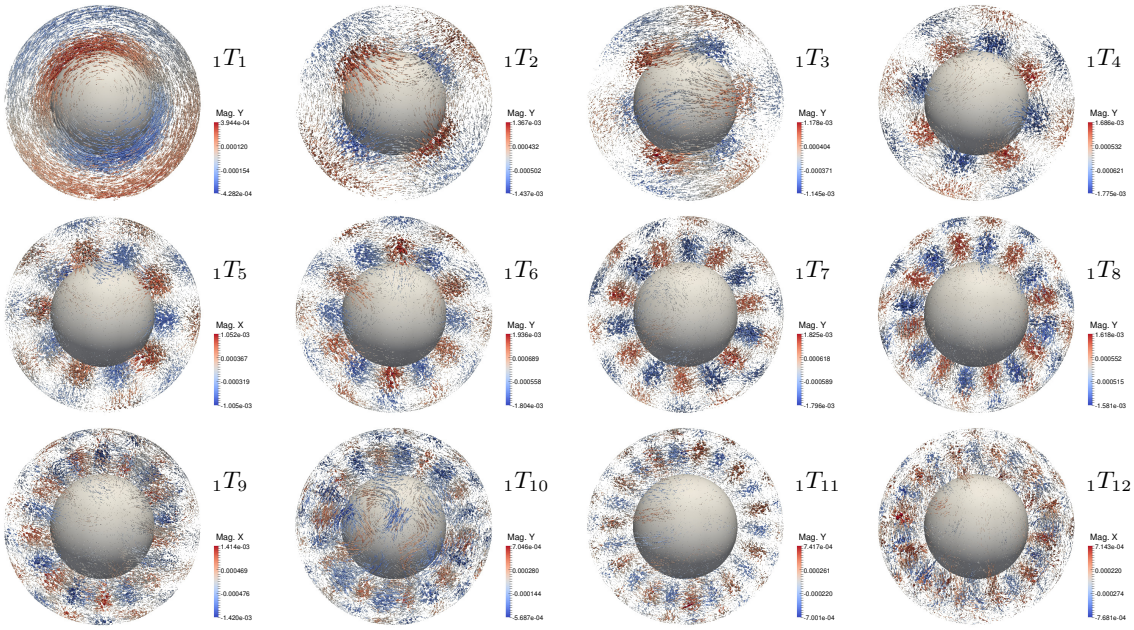

Figure B.7. Illustration of different toroidal modes with $n = 1$.

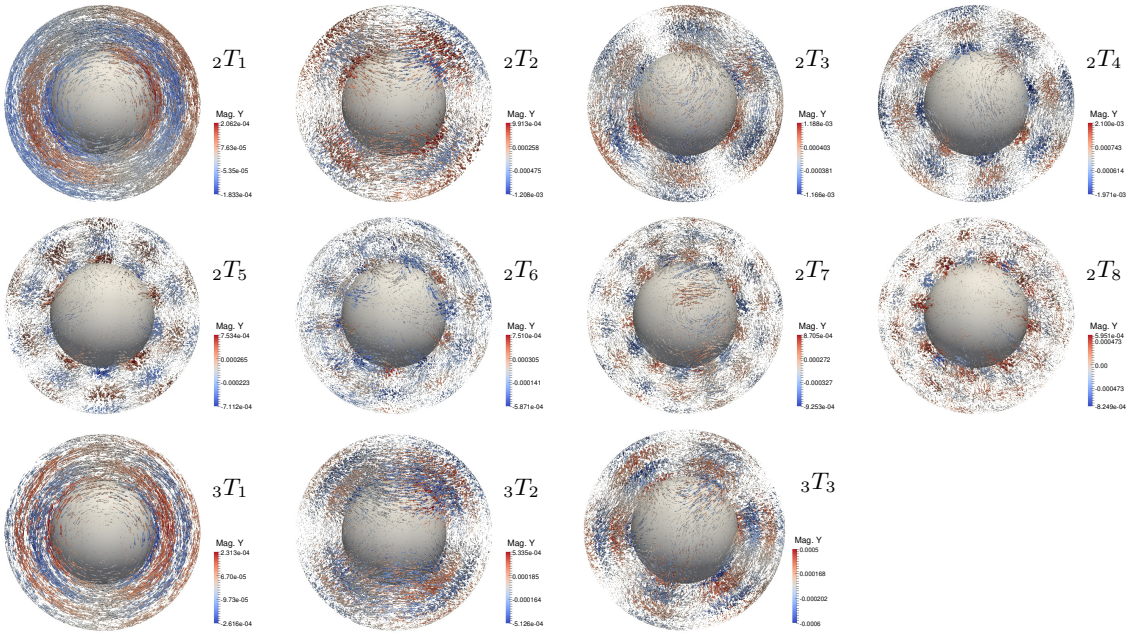

Figure B.8. Illustration of different toroidal modes with $n = 2, 3$.